ISSN 0027-1349, Moscow University Physics Bulletin, 2025, Vol. 80, No. 2, pp. 195–225. © Allerton Press, Inc., 2025.
Russian Text © The Author(s), 2025, published in Vestnik Moskovskogo Universiteta, Seriya 3: Fizika, Astronomiya, 2025, Vol. 80, No. 2, 2520301.

RADIOPHYSICS, ELECTRONICS, ACOUSTICS (REVIEWS)

Numerical Models of Nonlinear Acoustic Wave Propagation in Medical Ultrasound Problems and Certain Applications of Aeroacoustics and Underwater Acoustics

P. V. Yuldashev[1*], O. A. Sapozhnikov[2], M. M. Karzova[1], S. A. Tsysar[3], A. V. Kvashennikova[1], E. O. Konnova[3], and V. A. Khokhlova[2]**

[1]*Department of General Physics and Condensed Matter Physics, Faculty of Physics, Lomonosov Moscow State University, Moscow, 119991 Russia*

[2]*Department of Acoustics, Faculty of Physics, Lomonosov Moscow State University, Moscow, 119991 Russia*

[3]*Department of Photonics and Microwave Physics, Faculty of Physics, Lomonosov Moscow State University, Moscow, 119991 Russia*

Received September 16, 2024; revised November 17, 2024; accepted December 2, 2024

Abstract—The paper presents a review of numerical algorithms developed at the Laboratory of Medical and Industrial Ultrasound at Lomonosov Moscow State University, which are used to solve the evolution equations of nonlinear acoustics, such as the Burgers equation, the Khokhlov–Zabolotskaya–Kuznetsov (KZK) equation, and the one-way Westervelt equation. The main results obtained using these numerical models in studying the propagation of intense acoustic waves in various media are presented. In particular, examples of solving problems in medical ultrasound, nonlinear aeroacoustics, and nonlinear underwater acoustics are considered. The generalization of one-way models to account for medium inhomogeneities is discussed, employing wide-angle parabolic approximation methods in three-dimensional problems.

Keywords: numerical modeling, Burgers equation, KZK equation, Westervelt equation, medical ultrasound, nonlinear acoustic waves, inhomogeneous media, parametric array, wide-angle parabolic equation

DOI: 10.3103/S0027134925700316

INTRODUCTION

When addressing a wide range of problems in acoustics, it is essential first and foremost to determine the quantitative characteristics of the wave field generated in the medium by various transducers or sound sources. The equations describing the propagation of acoustic waves in liquids and gases incorporate a multitude of physical effects, such as diffraction, absorption and dispersion, scattering by medium inhomogeneities, and—in the case of high-intensity waves—nonlinear effects. These equations are quite complex, and in the general formulation of the problem, it is usually not possible to obtain analytical solutions for them. Therefore, in most cases, numerical modeling methods are employed, which allow one to obtain solutions for relatively arbitrary configurations of the medium and sound field sources. Moreover, the complexity of solving the problem depends on the complexity of the underlying equations and the approximations inherent in them. Typically, two main types of equations used in the numerical modeling of acoustic wave propagation can be distinguished.

First, there is a system of so-called full-wave equations of acoustics in liquids and gases, which can be obtained from the Navier–Stokes equations under certain assumptions [1]. Such a system most comprehensively takes into account all the physical effects associated with wave propagation, but at the same time, when solved numerically, it demands the greatest computational resources. In this approach, time acts as the evolution coordinate, and the numerical algorithms involve calculations that update the three-dimensional fields of various acoustic quantities (pressure, particle velocity, density), defined on discrete grids at each subsequent time step. Since the time step is linked to the spatial steps of the numerical grid by the Courant–Friedrichs–Lewy (CFL) criterion, the computational cost grows inversely proportional to the fourth power of the spatial grid step size. As a result, solving problems in the

*E-mail: petr@acs366.phys.msu.ru
**E-mail: helen.7aprel@gmail.com

presence of high-frequency components of the field becomes extremely resource-intensive. In particular, such a situation arises when nonlinear effects are taken into account, when the generation of higher harmonics of the fundamental emission frequency takes place. Currently, the most well known software implementation of this approach is the "k-Wave" numerical modeling package, which implements the ideas embedded in the full-wave model using the pseudospectral method [2].

Secondly, a large number of problems can be solved based on simplified equations in which various approximations were employed in the derivation process. For example, a physically justified simplification is the assumption of the one-way nature of wave propagation. Such a situation arises when a source sends waves into a half-space in the form of a directed wave beam, which is often implemented in various practical applications. By considering only forward-propagating waves, one can effectively eliminate one spatial dimension, thereby reducing the dimensionality of the problem by one. Namely, one of the spatial coordinates, chosen as the predominant direction of wave propagation, becomes the evolution variable due to the transition to a moving coordinate system. Thus, along this direction, the boundary-value problem is replaced by an initial-value problem, which is significantly simpler. The initial field is usually specified in a certain plane perpendicular to the axis of the evolution coordinate. The wave field is calculated sequentially, moving in a marching algorithm along the evolution coordinate from the current perpendicular plane to the next one with a certain step. In this case, the field in the moving coordinate system changes relatively slowly, which simplifies the application of numerical methods.

Examples of equations of this type in acoustics include the Burgers equation for one-dimensional finite-amplitude waves [3] and the Khokhlov–Zabolotskaya–Kuznetsov (KZK) equation for describing nonlinear wave beams [4]. The Westervelt equation [5], originally formulated to describe nonlinear waves propagating in all directions, can also be transformed into a one-way form. Methods of wide-angle parabolic approximation have developed extensively, being widely applied in aeroacoustics [6, 7], in underwater acoustics [8–10], and in other fields [11]. It is precisely equations of this type that were predominantly employed in solving numerous scientific problems at the Laboratory for Industrial and Medical Ultrasound of Lomonosov Moscow State University (LIMU, http://limu.msu.ru/). This is explained by the fact that the main interest lay in wave phenomena with strong manifestation of nonlinear effects and, owing to the complexity and cumbersomeness of the corresponding numerical problems, one-way models effectively became the only feasible option. In the present review, the main scientific directions of the Laboratory are highlighted, in which numerical modeling was performed using the aforementioned equations, namely, medical ultrasound, aeroacoustics, and parametric emission of low-frequency signals. Separately, the issue of generalizing one-way models to the case of an inhomogeneous medium in three-dimensional problems is discussed, employing methods of the wide-angle parabolic equation.

1. THEORETICAL MODELS AND NUMERICAL SCHEMES

1.1. Burgers Equation

For describing the propagation of plane (one-dimensional) finite-amplitude waves in a thermoviscous medium, the Burgers equation is often used:

$$\frac{\partial p}{\partial z} = \frac{\beta}{c_0^3 \rho_0} p \frac{\partial p}{\partial \tau} + \frac{\delta}{2c_0^3} \frac{\partial^2 p}{\partial \tau^2}. \qquad (1)$$

Here, p is the acoustic pressure, z is the evolutionary spatial coordinate, $\tau = t - z/c_0$ is time in the accompanying coordinate system, c_0 is the speed of sound, ρ_0 is the medium density, β is the nonlinearity coefficient, and δ is the thermoviscous absorption coefficient. The Burgers equation can also be modified for the cases of cylindrical and spherical waves [3]. Without thermoviscous absorption, the equation is known as the equation of simple waves:

$$\frac{\partial p}{\partial z} = \frac{\beta}{c_0^3 \rho_0} p \frac{\partial p}{\partial \tau}. \qquad (2)$$

Equations (1) and (2) have analytical solutions that are described in the relevant manuals [12]. However, they are not always convenient to use in practice due to the need to calculate integrals, and in many cases, it turns out to be simpler to obtain a solution by one or another numerical method on a discrete grid. Furthermore, in some problems, for example, in aeroacoustics, it is necessary to additionally account for the relaxation mechanism of absorption, which also precludes using the analytical solution for the general form of the waveform [13]. Since the Burgers equation is part of other nonlinear acoustic equations (for instance, the KZK equation), it makes sense to dwell in more detail on the main numerical methods for solving it.

By structure, in the right-hand side of the equation, there are two differential operators, one of which describes nonlinear effects responsible for the steepening of the waveform and the generation of higher harmonics of the fundamental frequency, while the

other describes thermoviscous absorption. In operator form, the equation can be written as

$$\frac{\partial p}{\partial z} = L_N p + L_A p, \tag{3}$$

where

$$L_N = \frac{\beta}{2c_0^3\rho_0}\frac{\partial (\cdot)^2}{\partial \tau} \tag{4}$$

is a nonlinear operator and

$$L_A = \frac{\delta}{2c_0^3}\frac{\partial^2}{\partial \tau^2} \tag{5}$$

is the operator of thermoviscous absorption.

Although it is in principle possible to construct a numerical scheme that takes into account the effect of the combined operator $L_N + L_A$ on the right-hand side, the splitting method [14, 15] is most frequently used. The idea of the method is to replace the computation of the solution of the equation at each small step Δz along the z-axis with the combined operator on the right-hand side (3) by a straightforward sequence of computations of the solutions to equations that have only one operator on the right-hand side, L_N or L_A. Most commonly, one encounters first-order and second-order accuracy schemes:

$$p(z+\Delta z) \approx L_{N,\Delta z} L_{A,\Delta z} p(z), \tag{6}$$

$$p(z+\Delta z) \approx L_{A,\Delta z/2} L_{N,\Delta z} L_{A,\Delta z/2} p(z), \tag{7}$$

where, the operators $L_{N,\Delta z}$ and $L_{A,\Delta z}$ describe the outcomes of solving the equations with the nonlinear operator and with the absorption operator, respectively, over a full step of the evolutionary coordinate Δz, while $L_{A,\Delta z/2}$ describes the solution of the equation with the absorption operator over a half step $\Delta z/2$. For the equation with the nonlinear operator, it is essentially necessary to solve the simple wave equation (2), and in the equation with the absorption operator, it is necessary to solve an equation that is equivalent in form to diffusion or heat-conduction equations. Since the operators of nonlinearity and absorption do not commute with each other, the error of this representation of the solution is proportional to $O(\Delta z^2)$ and $O(\Delta z^3)$ for first- and second-order accuracy schemes, respectively, and at sufficiently small Δz, it becomes negligibly small. The advantage of splitting schemes lies in the fact that for each operator, one can use the numerical scheme most suitable for it. Next, let us consider the main variants of the schemes used for both operators.

If the wave at the source is a harmonic signal with angular frequency ω_0, then it is more convenient to use a spectral approach in which the pressure function $p(\tau, z)$ is expanded into a finite Fourier series

$$p(\tau, z) = \sum_{n=-N}^{N} p_n \exp(in\omega_0\tau), \tag{8}$$

where N is the number of harmonics, and the amplitudes with negative indices are complex conjugates of the amplitudes with positive indices: $p_{-n} = p_n^*$. After substituting the Fourier expansion into the simple waves equation (2), one can write a system of nonlinear ordinary differential equations for the complex harmonics p_n:

$$\frac{\partial p_n}{\partial z} = \frac{i\beta n\omega_0}{c_0^3\rho_0} \times \left(\sum_{m=1}^{N-n} p_m^* p_{n+m} + \frac{1}{2}\sum_{m=1}^{n-1} p_m p_{n-m}\right). \tag{9}$$

Here, p_m^* is the complex conjugate of p_m. The system of equations (9) is solved by the standard fourth-order Runge–Kutta method, in which the number of computational operations in this case is proportional to the square of the number of harmonics [16]. Therefore, the method is efficient only when there is a small number of harmonics (a few dozen), sufficient for describing weakly distorted initially sinusoidal waveforms. When nonlinear effects strongly manifest themselves, resulting in the formation of a shock front in the waveform, the number of harmonics required in the numerical description grows to hundreds and thousands, and the method becomes extremely inefficient. To limit the number of harmonics in the spectral description of discontinuous waves, an asymptotic method was developed in which high-frequency components were included using an analytical result for the spectrum of a discontinuous wave. This method made it possible to describe the propagation of discontinuous waves using only 30 harmonics, but it was implemented solely for the one-dimensional case of plane wave propagation in an ideal medium and in a medium with an arbitrary frequency law of absorption and dispersion [16, 17]. In the general case of strongly nonlinear waves, it is advisable to use schemes formulated entirely in the time domain. Thus, in the program codes developed at LIMU, a conservative Godunov-type scheme presented in [18] is used. This scheme makes it possible to use only 1–2 time-grid points on the shock front and correctly describes the speed of the front's motion and the decrease in its amplitude over distance traveled.

The details of implementing the numerical scheme in the time domain can be found in [19]. This time-domain scheme is also better suited for describing

the propagation of pulsed signals, whose spectrum is initially very wide.

The thermoviscous absorption operator can be computed in the spectral representation using an exact analytical solution in the form of a decaying exponential:

$$p_n(z+\Delta z) = \exp\left(-\frac{\Delta z \delta \omega_0^2 n^2}{2c_0^3}\right) p_n(z). \quad (10)$$

This method is also applicable when the absorption operator takes a general form, for example, in the presence of an arbitrary number of relaxation processes (such as two relaxation processes for air) or in the case of a power-law frequency dependence of absorption (as in biological tissues). The corresponding absorption-related dispersion is likewise included in the analytical solution. In the time representation of the thermoviscous absorption operator, one can use well-known explicit and implicit finite-difference numerical schemes, usually formulated for heat conduction and diffusion equations.

It is also worth noting that if the pressure field representations for computing the nonlinearity and absorption operators do not match, then in the splitting scheme it is necessary at each step in the operator sequence to switch from the time representation to the spectral one and back again using the fast Fourier transform (FFT). This slightly increases the computation time but offers more convenience in selecting the most suitable combination of numerical schemes.

1.2. KZK and Westervelt Equations

Many physical phenomena observed in directed beams of nonlinear acoustic waves are explained by the combination of nonlinear and diffraction effects. Therefore, in realistic models, one must take into account not only nonlinearity but also diffraction effects, which are described in the evolutionary KZK equations

$$\frac{\partial^2 p}{\partial z \partial \tau} = \frac{c_0}{2}\left(\frac{\partial^2 p}{\partial x^2} + \frac{\partial^2 p}{\partial y^2}\right) + \frac{\beta}{2c_0^3\rho_0}\frac{\partial^2 p^2}{\partial \tau^2} + \frac{\delta}{2c_0^3}\frac{\partial^3 p}{\partial \tau^3} \quad (11)$$

and Westervelt equations:

$$\frac{\partial^2 p}{\partial z \partial \tau} = \frac{c_0}{2}\left(\frac{\partial^2 p}{\partial x^2} + \frac{\partial^2 p}{\partial y^2} + \frac{\partial^2 p}{\partial z^2}\right) + \frac{\beta}{2c_0^3\rho_0}\frac{\partial^2 p^2}{\partial \tau^2} + \frac{\delta}{2c_0^3}\frac{\partial^3 p}{\partial \tau^3}. \quad (12)$$

The same notation applies here as in the Burgers equation (1). The z axis of the Cartesian coordinate system is usually chosen to coincide with the beam axis and indicates the predominant direction of wave propagation in the beam. On the right-hand side of the KZK equation, the diffraction operator, which is proportional to the Laplacian in the transverse plane (x, y), appears first. In the Westervelt equation, the diffraction operator is proportional to the full Laplacian. These two equations on the right-hand side contain the same nonlinearity and absorption operators as in the Burgers equation. The equations are written for a homogeneous medium with constant sound speed and density. Accounting for inhomogeneities is a separate topic and is discussed at the end of the article. The main difference between the two equations is that in the KZK equation, diffraction effects are described in the parabolic approximation, which holds for small diffraction angles. It is commonly assumed that the accuracy of the parabolic equation is sufficient for diffraction angles of approximately up to 15 degrees relative to the beam axis [20, 21]. The actual angular range may vary depending on the specific problem being solved using the parabolic equation [22]. In the Westervelt equation, the diffraction operator is exact. This is evident from the fact that, upon discarding the nonlinearity and absorption operators, the Westervelt equation reduces to the usual linear wave equation, rewritten for the pressure field in the accompanying coordinate system.

When constructing numerical schemes for the two discussed equations, just as for the Burgers equation, one can employ a splitting scheme with respect to physical factors, with the only difference that instead of two operators, the scheme involves three operators describing the corresponding physical effects: nonlinearity, absorption, and diffraction [23]. The order of these operators can vary; however, in practice, the most frequently employed second-order version of the scheme is the one in which the sequence of operators begins and ends with the diffraction operator L_D, which computes the field for a half-step along the z axis [24]:

$$p(x,y,z+\Delta z) \approx L_{D,\Delta z/2} L_{A,\Delta z/2} L_{N,\Delta z} L_{A,\Delta z/2} \times L_{D,\Delta z/2} p(x,y,z). \quad (13)$$

It is easier to compute the diffraction operator in the spectral representation of the pressure field (8). For each Fourier harmonic p_n, in the case of the parabolic approximation in the three-dimensional variant of the KZK equation, it is necessary to solve the evolutionary equation:

$$\frac{\partial p_n}{\partial z} = \frac{1}{2ik_n}\left(\frac{\partial^2 p_n}{\partial x^2} + \frac{\partial^2 p_n}{\partial y^2}\right), \quad (14)$$

where $k_n = nk_0 = n\omega_0/c_0$ is the wave number at the angular frequency $\omega_n = n\omega_0$. This parabolic equation takes the form of a diffusion or heat-conduction equation with an imaginary coefficient and is typically solved using finite-difference schemes based on the alternating directions implicit method (the ADI method) in a rectangular domain in the (x, y) plane [25]. Various boundary conditions can be used at the edges of the computational domain, including the perfectly matched layer (PML) needed to damp spurious reflections when modeling beam diffraction in a free field.

The diffraction part of the Westervelt equation

$$\frac{\partial p_n}{\partial z} = \frac{1}{2ik_n}\left(\frac{\partial^2 p_n}{\partial x^2} + \frac{\partial^2 p_n}{\partial y^2} + \frac{\partial^2 p_n}{\partial z^2}\right) \qquad (15)$$

is not evolutionary, since it contains in the right-hand side, as part of the Laplacian, a second derivative with respect to z, and essentially represents the Helmholtz equation rewritten for the slowly varying amplitude p_n in the accompanying coordinate system. Therefore, the method used for the parabolic approximation is inapplicable here, and other approaches are necessary. In particular, since we are dealing with a homogeneous medium, the angle spectrum method is often employed, in which the pressure field of each harmonic $p_n(x, y, z)$ is expanded, using the Fourier transform, into a set of plane waves (the spatial or angular spectrum) described by the complex amplitudes $\widehat{p}_n(k_x, k_y, z)$ [26]. Here, k_x and k_y are the spatial frequencies along the corresponding axes and can be interpreted as the components of the wave vector of plane waves in the plane (x, y). In the spatial spectrum, the partial differential equation becomes a second-order ordinary differential equation with constant coefficients

$$\frac{\partial^2 \widehat{p}_n}{\partial z^2} + 2ik_n\frac{\partial \widehat{p}_n}{\partial z} - \left(k_x^2 + k_y^2\right)\widehat{p}_n = 0, \qquad (16)$$

which has two linearly independent solutions. One of them describes plane waves propagating into the half-space $z > 0$, and the other describes propagation in the opposite direction. Choosing only the solution for waves traveling in the direction $z > 0$ makes the model one-way. As a result, the complex amplitude of the plane wave with wave-vector components $\left(k_x, k_y, k_z = \sqrt{k_n^2 - k_x^2 - k_y^2}\right)$ at each subsequent step $z + \Delta z$ is calculated by multiplying the amplitude at the current step by an analytically specified coefficient, called the propagator [24]:

$$\widehat{p}_n(k_x, k_y, z + \Delta z) = \exp\left(i\Delta z\sqrt{k_n^2 - k_x^2 - k_y^2} - ik_n\Delta z\right) \times \widehat{p}_n(k_x, k_y, z). \qquad (17)$$

Note that this solution includes not only propagating plane waves with $k_z > 0$, but also evanescent waves with imaginary k_z, which decay exponentially along the z-axis. Transforming from the spatial spectrum back to coordinate space yields the resulting field at the next step.

The pressure field is usually given on a two-dimensional rectangular grid, and from a computational standpoint, the angle spectrum method proves efficient due to the use of a fast discrete Fourier transform for two-dimensional matrices. On the other hand, the discrete nature of the spatial spectrum leads to certain artifacts [24], associated with the effect of periodically continued fields in coordinate space; the degree of these artifacts can be reduced by various types of spatial spectrum filtering [27].

In addition to the three-dimensional KZK and Westervelt equations, in some cases it can be practical to use their versions for axially symmetric fields, which are simpler to solve numerically because the number of dimensions is effectively one less. Then, instead of equations (14) and (15) to compute diffraction, one must solve analogous equations with the corresponding radially symmetric Laplacian:

$$\frac{\partial p_n}{\partial z} = \frac{1}{2ik_n}\left(\frac{\partial^2 p_n}{\partial r^2} + \frac{1}{r}\frac{\partial p_n}{\partial r}\right), \qquad (18)$$

$$\frac{\partial p_n}{\partial z} = \frac{1}{2ik_n}\left(\frac{\partial^2 p_n}{\partial r^2} + \frac{1}{r}\frac{\partial p_n}{\partial r} + \frac{\partial^2 p_n}{\partial z^2}\right), \qquad (19)$$

where $r = \sqrt{x^2 + y^2}$ is the radial coordinate of the cylindrical coordinate system (r, z). The radially symmetric parabolic diffraction equation (18) can be solved using finite-difference schemes, for example, the Crank–Nicolson scheme, which is written after applying the approximations $\partial p_n/\partial z \approx \left(p_n^{m+1} - p_n^m\right)/\Delta z$ for the evolutionary derivative on the left-hand side, and $p_n \approx \left(p_n^{m+1} + p_n^m\right)/2$ for the field on the right-hand side. Here, the notations $p_n^{m+1} = p_n(z + \Delta z, r)$ and $p_n^m = p_n(z, r)$ are used for the fields at the next and current steps. After rearranging the terms, the equation takes the form:

$$\left(1 - \frac{i\Delta z}{4k_n}\left(\frac{\partial^2}{\partial r^2} + \frac{1}{r}\frac{\partial}{\partial r}\right)\right)p_n^{m+1} = \left(1 + \frac{i\Delta z}{4k_n}\left(\frac{\partial^2}{\partial r^2} + \frac{1}{r}\frac{\partial}{\partial r}\right)\right)p_n^m. \qquad (20)$$

Discretizing the radially symmetric Laplacian on the grid in r, for example using a second-order finite-difference method, yields a final system of linear equations with a tridiagonal matrix, which is solved by the Thomas algorithm. Boundary conditions in the form of a PML can also be used at the edges of the computational domain.

To solve Eq. (19), corresponding to the diffraction part of the Westervelt equation, the angle spectrum method can also be applied, as in the three-dimensional case [28]. However, to expand the field into the spatial spectrum, instead of a two-dimensional discrete Fourier transform, one must use the discrete Hankel transform, for which in a direct implementation, the number of operations is proportional to the square of the number of spatial spectrum components, and there is no fast FFT-like version of the algorithm. Therefore, in the axially symmetric case, it is far more efficient to employ the wide-angle parabolic equation formalism [29], within which one can build finite-difference numerical schemes structurally similar to those for the narrow-angle parabolic equation [30]. In that case, the one-way equation for the harmonic p_n is written as

$$\frac{\partial p_n}{\partial z} = ik_n\left(\sqrt{1+\frac{\Delta_\perp}{k_n^2}}-1\right)p_n, \qquad (21)$$

where, for brevity, the transverse Laplacian operator is denoted as

$$\Delta_\perp = \frac{\partial^2}{\partial r^2}+\frac{1}{r}\frac{\partial}{\partial r}. \qquad (22)$$

This formulation employs the pseudodifferential operator $\sqrt{1+\Delta_\perp/k_n^2}$. A formal solution of equation (21) is expressed by means of the propagation operator [31]:

$$p_n(r,z+\Delta z) = \exp\left[ik_n\Delta z\left(\sqrt{1+\frac{\Delta_\perp}{k_n^2}}-1\right)\right]p_n(r,z). \qquad (23)$$

The exponential propagator can be computed approximately using (N_l, N_l) Padé approximations [32]:

$$p_n(r,z+\Delta z) = \prod_{l=1}^{N_l}\frac{1+\mu_l\Delta_\perp/k_n^2}{1+\nu_l\Delta_\perp/k_n^2}p_n(r,z). \qquad (24)$$

Here, the coefficients μ_l and ν_l are functions of the parameter $ik_n\Delta z$ (the dimensionless step) and are determined based on considerations of stability and accuracy in approximating the original propagator [33]. In practice, even though the propagator is computed approximately, usually only a small number N_l (for example, $N_l = 3$) in the product of operators in Eq. (24) is needed to ensure very high approximation accuracy for steps Δz comparable to or even exceeding the wavelength. Calculating the field at each subsequent step reduces to solving a chain of equations of the form

$$\left(1+\nu_l\Delta_\perp/k_n^2\right)p_n^{(l+1)} = \left(1+\mu_l\Delta_\perp/k_n^2\right)p_n^{(l)} \qquad (25)$$

for the indices $l = 1,\ldots,N_l$, where the sequence is initiated by the field at the current step $p_n^{(1)} = p_n(r,z)$, and the result of the entire chain of equations is the field at the next step $p_n^{(N_l+1)} = p_n(r,z+\Delta z)$. Other than the coefficients before the Laplacian in the left- and right-hand sides, these equations do not differ from Eq. (20), and constructing a finite-difference numerical scheme for them is entirely analogous to the standard Crank–Nicolson scheme for the narrow-angle parabolic equation.

The equations and methods of solution described above underlie various separate programs and software packages developed at LIMU for a wide range of problems related to the propagation of nonlinear acoustic waves. The specific implementation of the numerical methods is typically adapted to the particular features of each problem by making physically justified assumptions, as will be mentioned in the relevant sections of the article. Here, it is only worth noting that the presented numerical methods and algorithms are well suited to parallelization for execution on multicore processors. For example, the nonlinearity and absorption operators can be calculated independently and in parallel for different points on the spatial grid. In nonlinear problems, the diffraction operator is computed in parallel for individual Fourier harmonics p_n. In the angle spectrum method, parallelization of calculations for each harmonic p_n can be accomplished using parallel versions of the FFT algorithm. At present, work is underway to accelerate computations by taking advantage of graphics processing units [34].

2. MEDICAL ULTRASOUND

2.1. Three-Dimensional Model Based on the Westervelt Equation for Medical Ultrasound

Although the development of medical applications of ultrasound began quite some time ago, intensive research in this field continues to this day [35]. This is due to the emergence of new technologies and hardware capabilities, as well as the expanding range of ultrasound applications in medicine [36]. For instance, in addition to the classic thermal ablation of organs and tissues used in implementing the method of noninvasive ultrasound surgery [37], promising protocols have been developed involving shock-wave pulses, known collectively under the name histotripsy [38, 39].

Numerical experiment plays a major role in the advancement of medical ultrasound methods. Thus, in developing various protocols for ultrasound exposure on the biological tissues of the body in order to assess the safety and effectiveness of a planned procedure, one must know in advance the distribution of the wave

field generated in the medium by the chosen transducer. Numerical experiment makes it possible to analyze the situation over a wide range of parameter values for the problem and to select the configuration of the transducer that best suits the specified goals. At the same time, numerical experiment can circumvent many of the limitations present in purely experimental methods of studying fields and compute the required quantities throughout the entire region of interest in space. For example, the finite frequency band and finite size of measurement sensors (hydrophones) can significantly distort the waveform being investigated, whereas in numerical modeling one can obtain the desired signals practically without distortion [40].

A substantial volume of work carried out at LIMU on the topic of medical ultrasound using numerical modeling methods was aimed at creating methods of quantitative characterization of the fields of powerful, strongly focused transducers developed primarily for noninvasive ultrasound surgery applications. Of particular interest were modes of operation of the transducers at high intensities of the ultrasound field, sufficient for the formation of shock fronts in the focal region. This relates to the development of new protocols for irradiating biological tissues based on the histotripsy method [41] and to improvements in thermal ablation methods [42]. Accordingly, a combined technique was developed, based on numerical modeling of nonlinear acoustic equations and on experimental data obtained when scanning the field with a hydrophone in the method of acoustic holography and directly measuring high-intensity fields with a fiber-optic hydrophone. Initially, this method was tested on radially symmetric fields using the KZK equation [43], and then it was extended to three-dimensional fields using a numerical model based on the Westervelt equation [44]. Both the theoretical and the experimental components of the method require additional explanation here.

Although the individual elements of the three-dimensional Westervelt equation solution algorithm described in the previous section are fairly straightforward and well-studied, its direct application to modeling strongly nonlinear ultrasound fields with shock fronts leads to unrealistically high memory requirements and lengthy computations. This is due both to the large number of harmonics needed to accurately describe waves with discontinuities and to the increased requirements on the spatial resolution of the numerical grid in the transverse plane, since the focal region size for focused nonlinear waves is smaller compared to the linear case. Therefore, a physically justified optimization was proposed, related to the spatial characteristics of the focused fields of typical transducers for noninvasive ultrasound surgery [45]. Specifically, because nonlinear effects depend on amplitude, as the wave field intensity increases, they begin to manifest earlier where the amplitude in the wave beam is highest, i.e., in a small region around the focus. As a result, in all practically realizable high-power irradiation regimes, shock fronts are also formed near the focus. In the rest of the space, the field remains quasi-linear, i.e., it has a waveform only slightly different from a sinusoid, which can be described using a small number of harmonics. This allows for storing a large number of harmonics (on the order of a thousand) in relatively small arrays corresponding to the numerical grid that covers the focal spot with sufficient overlap, while for the rest of the space using arrays with a greatly reduced number of harmonics (several dozen or hundreds). As a result of this optimization, the total size of the arrays was reduced by more than an order of magnitude, and the computation time was brought down to reasonable values of a few dozen hours (taking into account parallel computations on multicore processors). Additionally, artificial absorption was introduced in the numerical scheme, activated locally at the points of the spatial grid where shock fronts formed. This made it possible to maintain the specified shock front width (usually 8–9 grid points per discontinuity) and to reduce transverse spatial gradients of the pressure field in order to smooth out spurious oscillations in the waveform.

Acoustic holography, which is the second component of the method, refers to experimental techniques for investigating wave fields and plays an important role in matching the developed numerical model to the description of fields of real transducers [47]. It is worth noting here that creating ultrasonic transducers for specific applications is itself a complex scientific and technical challenge, requiring numerous design approaches and various materials. Therefore, it is often impossible to model the operation of an transducer starting from its geometry and design, because the details of its implementation (physical parameters of materials, the placement of emitting elements, electrodes, etc.) are either not precisely known or constitute a trade secret, while the equations accounting for piezoelastic effects in solids and their solution methods are quite complicated. Acoustic holography avoids many of these difficulties and abstracts away from most design details by obtaining complete information on the resulting field generated by the transducer in the medium.

One convenient way to implement acoustic holography is the synthetic aperture method. For this purpose, using a hydrophone, one records the spatial distribution of pressure on a certain surface (usually a plane perpendicular to the beam axis, although surfaces of other geometries can also be used [48]) when

the transducer operates in specified modes in water. The scanned distributions of amplitude and phase in a set of discrete points on the plane in monochromatic mode collectively form the hologram, which can be used to reconstruct the field in any region of space of interest, under the assumption of linear wave propagation. When considering pulsed signals, one can, using a time-frequency Fourier transform, obtain sets of monochromatic holograms (so-called pulsed or nonstationary holograms) for a particular frequency band all at once [49]. To transfer the field onto the required surface, one employs numerical models based on the angle spectrum method (from plane to plane) or on calculating the Rayleigh integral (for curved surfaces) [47].

In numerical modeling of powerful ultrasound fields, the hologram is used to specify the initial conditions for the one-way wave model [44]. In this case, the hologram is recorded at some distance from the source, and then linearly propagated back to the plane attached to the transducer. For example, if the transducer is made on a segment of a spherical surface, this might be the tangent plane at the apex of that surface. The hologram is usually recorded at a sufficiently low acoustic power of the beam, at which the field can be regarded as almost linear. When the transducer drive power is increased, the hologram is rescaled in amplitude by a factor determined from additional hydrophone measurements at some point in the near field. Hence, there is no need to account for the coefficient of conversion of electrical power supplied to the transducer into the acoustic power of the beam, which, generally speaking, varies depending on the device's operating mode.

Acoustic holography has been developing in the laboratory as a research direction in its own right, and a number of important results have been obtained in biomedical ultrasound applications. In particular, one can reconstruct the amplitude and phase of the particle velocity on the surface of the transducer (Fig. 1), for example, to detect defects indicated by a low amplitude of oscillations in some area [50], or by phase deviations, which is convenient in characterizing multielement transducers [51]. Moreover, the method allows one to identify and compensate for inaccuracies in the relative positioning of the hologram surface and the transducer [52], as well as deviations of the positioning system's axes from orthogonality [53]. For multielement transducers, it was proposed to record holograms of individual elements, which can subsequently be combined in numerical modeling to analyze the electronic focusing capabilities by adding the corresponding phases to the signals fed to individual elements [54]. Measuring the total beam power by leveraging the radiation force effect, together with the hologram data, enables absolute hydrophone calibration [55]. Reconstructing the phase on the spherical surface of a multielement transducer based on holography data is used to correct shape defects introduced during manufacturing, since in practice it deviates from the ideal sphere [56]. The correction, applied as an additional phase on the elements, improves the wave beam focusing. Using the holographic approach to determine the full beam structure allows one to decompose the field into a set of true plane waves even for focused beams, which is employed in determining the acoustic characteristics of materials of small volume, relevant for biological samples [57].

Using the combined technique described above, the fields of a large number of medical ultrasound transducers of various designs were analyzed. In doing so, the modeling results were compared with measurements of waveforms at the focus made using a fiber-optic hydrophone, which has absolute calibration and a wide frequency band sufficient to reproduce waveforms with shock fronts. For example, it was shown that the field generated in water by a 256-element array of a commercial ultrasound surgery system (Sonalleve V1 3.0T, Philips Healthcare) is well described within this model over the entire accessible range of powers, including regimes in which a shock front forms with amplitudes up to 100 MPa at the focus [44]. Similar results were obtained for several prototypes of large multielement arrays developed for the boiling histotripsy method [58, 59]. For other applications, the nonlinear fields of diagnostic transducers in the form of one-dimensional linear arrays were investigated. Such arrays can operate in a combined mode both for providing therapeutic impact and simultaneously for acquiring a diagnostic image. For instance, it was shown that for a standard 128-element commercial diagnostic transducer C5-2 operating at a frequency of 2.3 MHz, which in a high-power short-pulse mode was tested in the development of a kidney stone pushing protocol based on the radiation force effect, shock fronts can form at the focus [60]. In this case, when all 128 elements were activated, there was a significant discrepancy between the modeling and experimental results, which was explained by the fact that with tight beam focusing, the focal region became comparable in size to the diameter of the hydrophone's sensitive element (optical fiber), and an averaging effect was observed. This result indicates that numerical modeling supported by experimental data can yield more reliable outcomes than purely experimental methods of investigation. Another one-dimensional 64-element array at 1 MHz was developed for implementing pulsed high-intensity ultrasound techniques. For example, this method is used to initiate inertial cavitation in

tissue for targeted drug delivery without introducing contrast agents (bubbles with an artificial shell). Numerical modeling first made it possible to determine the optimal design of the transducer that provides the necessary ultrasound field parameters under specified constraints on the transducer geometry and the maximum allowable power [61]. Subsequently, a prototype device was fabricated, its operation characterized at the specified powers, the possibilities of electronically shifting the focus analyzed, and the quality of the diagnostic image evaluated [62].

The three-dimensional model based on the Westervelt equation was also employed for theoretical analysis of histotripsy protocols for exposure to biological tissues. Thus, using a combined approach consisting of jointly applying the full-wave model "k-Wave" and the Westervelt equation, the propagation of a powerful focused ultrasound beam through an intact skull into brain tissue was calculated [63]. In this problem, the entire modeling region was divided into three subregions: from the transducer to the skull, a homogeneous subregion with water; then a subregion containing a segment of the inhomogeneous skull; and finally a subregion containing brain tissue, assumed homogeneous. Such a partitioning allowed one to compute nonlinear wave propagation in the homogeneous subregions based on the Westervelt equation, while the inhomogeneities and irregularities of the skull surface, and the aberrations they cause, were accounted for by the linear "k-Wave" model. Physically, splitting into a combination of linear and nonlinear models is justified by the fact that skull bones are a highly absorbing medium and almost do not transmit the high harmonics generated by nonlinearity in the first subregion on the path from the transducer to the skull. As a result, it was found that, taking into account aberration compensation based on the capabilities of a 256-element array with a tightly packed arrangement of elements, and given existing technical constraints on the maximum ultrasound intensity at the transducer surface ($40\ \mathrm{W/cm^2}$), it is possible to achieve shock fronts in the brain tissue with amplitudes exceeding 60 MPa at the focus, and thus to implement histotripsy mechanisms of tissue treatment.

Another example of using the three-dimensional nonlinear model relates to studying the focusing of ultrasound beams in liver tissue in the presence of ribs [64]. Here, the problem is that the ribs block part of the beam and, due to the alternating structure of the open window, create a kind of diffraction grating. When a multielement array is used, some of the elements are turned off so that the ultrasound beam primarily passes through the gap between the ribs, avoiding excessive heating of the tissues around them. As a result, not only is the field at the focus attenuated, but additional diffraction maxima appear, degrading the localization of the therapeutic effect of the ultrasound. In the cited work, the process of thermal ablation of tissue was examined, and it was shown that by increasing the ultrasound intensity at the transducer, one can improve the localization of thermal sources at the main focus via nonlinear effects. In that case, the outcome is achieved because nonlinear effects begin to appear earlier in the main focus than in the side maxima, whose amplitude is initially smaller. Hence, the onset of shock fronts, accompanied by a significant increase in heat release, also occurs earlier in the main focus.

2.2. A Radially Symmetric Model Based on the KZK and Westervelt Equations in Medical Ultrasound Problems

As already mentioned above, even when all optimizations are introduced into the algorithms for solving the three-dimensional Westervelt equation, the computation with a single specific set of input parameters for the numerical model takes a significant amount of time (tens of hours) on high-performance servers and workstations with multicore processors. In connection with this, a simplified numerical model was developed at LIMU based on radially symmetric versions of the KZK and Westervelt equations (using the wide-angle approximation to compute the diffraction operator). The numerical model is equipped with a graphical user interface and is made available for free use on the LIMU website as a software package (Fig. 2a) under the name "HIFU-beam" [65] (an abbreviation for high intensity focused ultrasound beam). Using "HIFU-beam," one can compute the fields of single-element focused transducers (Fig. 2b) and ring arrays (Fig. 2c), fabricated on a segment of a spherical surface, in a homogeneous medium or a medium consisting of several planar layers arranged perpendicular to the beam axis. In this case, such layers can be used to simulate ultrasound propagation in biological tissue, which, to a rough approximation, also consists of layers: skin, fat, muscle, organs, and so forth. The radially symmetric model has several applications in which independent results have been obtained.

First, it serves for analyzing the fields of radially symmetric transducers (Fig. 2d), which are often used in medical ultrasound laboratories when there is no need for more expensive and complex devices, such as multielement arrays with a three-dimensional field structure. For example, in addition to single-element transducers, ring arrays are employed, which, through electronic focusing, provide shifting of the focal maximum along the axis. A negative consequence of electronic focusing is the

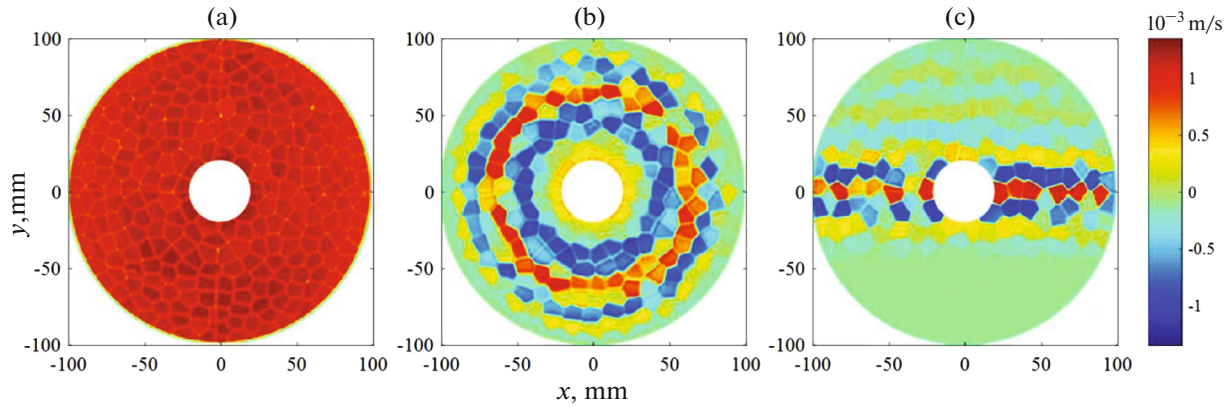

Fig. 1. The distributions of the normal component of the vibrational velocity on the surface of a 256-element piezocomposite spherical transducer, obtained using the acoustic holography method, are presented for a central frequency of 1.2 MHz, an aperture of 200 mm, and a curvature radius of 150 mm under different focusing conditions: (a) when emitting short pulses focused at the geometric focal point, (b) with an electronic focus shift along the axis by 15 mm from the transducer, and (c) with an electronic focus shift by 8 mm perpendicular to the axis.

formation of secondary diffraction maxima in the prefocal and postfocal regions, which can be quite strong due to the regular structure of ring arrays. For a 12-element ring array operating at 2 MHz, available in the laboratory, the influence of electronically shifting the focus along the beam axis on the formation of shock fronts in the main and secondary maxima was examined based on the wide-angle model [46]. Safe distances were determined for which one can move the focus away from its original position, set by the radius of curvature of the spherical surface, and it was also shown that in some cases, to change the beam's focusing angle, it can be more advantageous to turn off the outer elements rather than phase the array with all elements turned on. In another study using the KZK equation, a characterization was carried out for a radially symmetric transducer of the Duolith SD1 medical extracorporeal shock-wave therapy device [66]. Modeling demonstrated that although nonlinear effects appear in the field generated by this device, shock fronts are still not formed.

Second, using the radially symmetric model based on the KZK equation, the general properties of nonlinear focused beams and the limiting values of parameters of discontinuous waves attained at the focus were investigated. Although analytical estimates for the limiting pressure level at the focus, obtained from various approximations, have long been known [67, 68], numerical modeling makes it possible to obtain specific numerical values with high accuracy. Thus, for focused piston transducers, saturation curves were obtained for the positive and negative pressures and intensity at the focus, depending on the transducer's gain when focusing linear waves [69]. They are called saturation curves because, when the amplitude of the initial acoustic wave is increased, the levels of positive and negative pressure at the focus vary in a nonlinear manner (Fig. 2e). For peak positive pressure, there is initially a rise that is faster than a linear dependence, associated with better focusing of higher harmonics, and then the rise slows dramatically because of limiting factors that arise when a discontinuity wave forms: additional nonlinear absorption at the shock front or nonlinear refraction [70]. Peak negative pressure grows more slowly in magnitude than a linear dependence would predict. It is shown that the analytical estimates and the results of the numerical calculation coincide in order of magnitude, though the error in the analytical expressions is still too large for practical use. For pulsed and periodic fields of a Gaussian beam, the physical mechanisms that cause saturation of the field at the focus were studied separately [71]. It was shown that for periodic waves, the saturation of wave parameters at the focus occurs mainly due to nonlinear absorption at the shock front. In pulsed fields, pressure saturation is more related to the manifestation of nonlinear refraction. As a result, the limiting values of peak positive pressure in periodic fields turn out to be higher than in pulsed fields. As the beam power increases, shock front formation at the focus takes place at a certain intensity level, after which the front amplitude rapidly grows, transitioning to saturation at higher powers. For practical purposes, it was proposed to mark the onset of saturation by the formation of what is known as a fully developed discontinuity, which corresponds to the maximum dimensionless discontinuity amplitude, i.e., the amplitude referenced to the pressure at the source [72]. Visually, a fully developed discontinuity forms when the peak positive pressure becomes equal to the discontinuity amplitude (Fig. 2f). An transducer operating in the regime of fully developed discontinuities is best suited for implementing protocols that expose

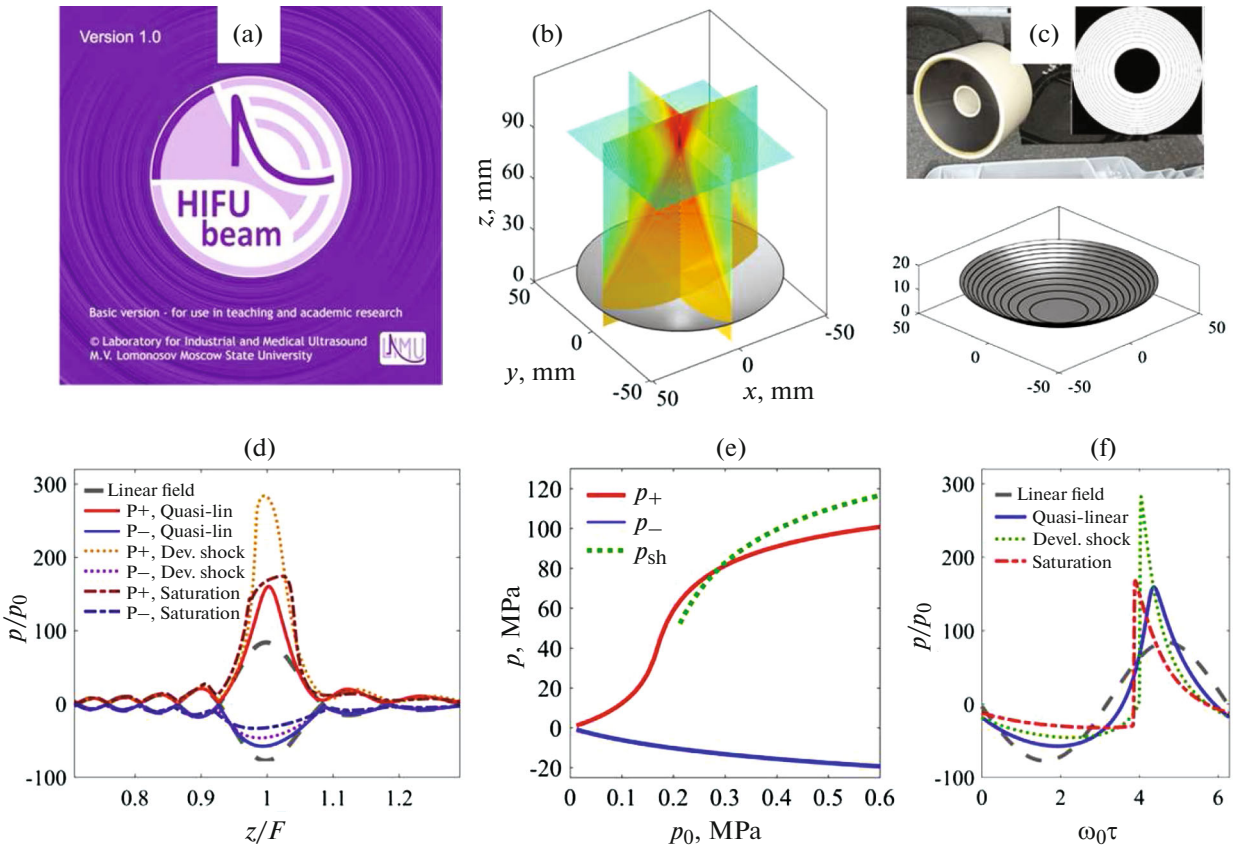

Fig. 2. Modeling of radially symmetric nonlinear ultrasonic beams: (a) program logo with a graphical user interface for "HIFU-beam," (b) 3D model and field of a single-element focused transducer, (c) photograph and 3D model of a ring array, (d) positive $P_+ = p_+/p_0$ and negative $P_- = p_-/p_0$ dimensionless pressure of the wave field on the axis of a single-element transducer (focus $F = 120$ mm, diameter $D = 120$ mm, frequency $f_0 = 1.2$ MHz) for three characteristic operating regimes: quasi-linear, fully developed shock at focus, and saturation (where $p_0 = \rho_0 c_0 u_0$ is the characteristic pressure at the transducer, related to the amplitude of the surface oscillation velocity u_0), (e) dependences of p_+, p_-, and shock front amplitude p_{sh} in absolute values (MPa) on the transducer pressure p_0 (saturation curves), (f) dimensionless waveforms p/p_0 for the three characteristic operating regimes: quasi-linear, fully developed shock at focus, and saturation.

biological tissue using shock-wave pulses. Therefore, the inverse problem was posed of determining the necessary parameters of an transducer to create a fully developed discontinuity of the required magnitude in the medium. To this end, multiparameter forward modeling of the focusing of a nonlinear ultrasound beam generated by a piston transducer was carried out, based on the radially symmetric KZK equation [72]. From analyzing a broad dataset, it was found that if the transducer's wave size is large (which in practical medical ultrasound applications is almost always the case), the amplitude of the fully developed discontinuity is determined primarily by the transducer's focusing angle or the so-called aperture number $F_{\text{number}} = F/D$, where F is the focal distance and D is the transducer diameter. As the focusing angle increases and F_{number} decreases, the amplitude of the fully developed discontinuity grows, and for $F_{\text{number}} = 1$, it reaches about 80 MPa in water. The corresponding curves of the discontinuity amplitude and peak positive and negative pressures versus F_{number} were constructed, and the required acoustic power of the beam was also determined.

Third, the results obtained in analyzing the focusing of radially symmetric nonlinear beams can also be applied to estimating fields with a three-dimensional structure, for example, those created by multielement randomized arrays. For this purpose, the concept of an equivalent axisymmetric transducer was introduced, whose linear field provides a good approximation of the real transducer's field in the region of the focal maximum [73]. Since, when linear fields are close in geometry and amplitude, nonlinear effects will develop almost identically, the fields will also be similar at high intensities. This is explained by the fact that nonlinear effects manifest chiefly where the field amplitude is highest, i.e., at the focus, where the approximation by the field of the equivalent source is most accurate. By using several arrays as an example, it was shown that the results of numerical modeling

employing the three-dimensional Westervelt equation with holographic initial conditions and the radially symmetric KZK equation for suitably chosen equivalent sources agree well, confirming the viability of this method [74].

The data obtained in the radially symmetric model can be used for a quick evaluation of the capabilities of a given transducer in protocols for exposure using shock-wave pulses, such as in histotripsy [75, 76]. In particular, the equivalent source method was used in exploring the potential feasibility of applying multi-element focusing transducers to implement the histotripsy method in noninvasive surgery of deep regions of the brain through an intact skull [77]. Here, the field of an arbitrary array on a spherical segment was replaced by an equivalent source, taking into account the fill factor of the array's surface by emitting elements. Assuming the aberrations on skull-bone inhomogeneities are compensated, and with reflection and absorption losses factored in, it was found that implementing a histotripsy exposure while adhering to the technical constraints on element intensities is feasible for arrays with dense fill at ultrasound frequencies around 1 MHz, with an aperture number $F_{\text{number}} = 1$ and the transducer diameter of about 20 cm.

Furthermore, when examining nonlinear focused beams, interesting physical effects are observed, which can be conveniently studied in radially symmetric models. In the linear case, the field on the axis of a piston transducer beam can be represented as the sum of a direct wave and an edge When nonlinear effects strongly manifest, each of these waves near the focus forms a shock front [79]. The fronts are oriented toward each other at some angle, depending on the transducer's focusing angle. These two fronts, in general, travel at different speeds and at some instant "collide" with each other near the beam axis, forming a single new shock front with a larger amplitude. The incident and reflected wave fronts do not meet at the surface; rather, they merge at some point above it, from which a "Mach stem" descends to the surface. Here, the identical nature of nonlinear-diffraction effects in two different physical problems is explained by the fact that, on the axis of a radially symmetric beam, the same boundary condition is satisfied as in reflection from an absolutely rigid surface: zero normal derivative of the pressure at the surface. On the plot of peak positive pressure versus distance along the axis, the formation of a "Mach stem" in a strongly nonlinear focused beam is revealed by a small local peak located before the main focal maximum [65]. The point is that after a shock front of higher amplitude forms in the "Mach stem," exceeding that of the two original waves, there is a sharp increase in nonlinear absorption, which is proportional to the cube of the shock front amplitude. Therefore, the front's amplitude begins to decrease more rapidly than it did prior to the collision of the two original fronts shortly before reaching the focus. Then, the front amplitude recovers and reaches a maximum, since some distance still remains before the focus.

3. AEROACOUSTICS

3.1. Nonlinear Pulses in a Randomly Inhomogeneous Medium

Research in nonlinear aeroacoustics conducted in the laboratory was largely motivated by the problem of impulsive noise generated by civil supersonic aircraft. Noise waves propagate from a supersonic aircraft in the form of a Mach cone and are perceived on the ground as very sharp impulsive noise, causing annoyance [81]. The classical shape of such a pulse is known in the literature as an "N-wave," as it consists of two steep fronts—a leading and a trailing one—connected by a linear section, resembling the letter "N." It is the asymptotic form of a finite-amplitude wave that emerges during its extended propagation in the atmosphere due to nonlinear effects following the merging of numerous small steep fronts from the initial aerodynamic disturbance generated near the aircraft's fuselage. Currently, the shape of planned commercial supersonic aircraft is optimized to reduce the magnitude of the pressure jump on steep sections of the waveform by "spreading" the impulse in time, significantly reducing noise levels [82]. Such waveforms are discussed in the literature under the term "low-boom" and are currently actively studied.

Among many aspects of this problem, the laboratory studied the propagation of an N-wave through the near-ground turbulent atmospheric layer. The specificity of these processes lies in the fact that at altitudes up to 1–2 km, atmospheric instability leads to various forms of turbulence, such as vortices in strong winds or temperature fluctuations in ascending convective flows over a heated ground surface. As a result, the speed of sound above the ground experiences small fluctuations occurring at different scales, significantly influencing acoustic wave propagation. For example, the random spatial distribution of sound speed, which can be metaphorically viewed as numerous scattered acoustic "lenses" of varying sizes and strengths, leads to random focusing and defocusing of the wave field, where wave amplitude and consequently noise levels are randomly amplified or attenuated [83]. Therefore, the problem typically involves studying the statistical characteristics of the wave field after passing through a turbulent layer of a

given thickness and intensity. In general, wave propagation in randomly inhomogeneous media is extensively documented since it appears across numerous fields in wave physics [84]. However, the pronounced nonlinear effects and impulsive nature of the wave field distinguish this particular problem, influencing the choice of investigation methods. Due to the impossibility of obtaining exact analytical solutions to the corresponding nonlinear wave equations in a randomly inhomogeneous medium, numerical methods are primarily employed.

In earlier studies in the laboratory, the phase-screen model was used to represent the randomly inhomogeneous medium [85]. This model is advantageous because it allows an analytical interpretation of solutions within the geometric acoustics method. However, the geometric method leads to singularities in the acoustic field upon caustic formation, which must be described separately [86]. Furthermore, a single phase screen specifies random perturbations of the wavefront only at an initial plane [87], although, in reality, these fluctuations gradually accumulate as the wave propagates deeper into the inhomogeneous medium. Therefore, it is more realistic to use equations that account for diffraction along with distributed inhomogeneities in sound speed and medium velocity (in the presence of wind). In the most general formulation, even one-way equations and methods of their solution turn out to be quite complicated, as they include numerous differential operators responsible for describing wave propagation in an inhomogeneous moving medium [88]. It is also necessary to consider the general geometry of the incident wavefront (Mach cone) and atmospheric stratification [89]. For example, a vertical gradient of sound speed results in different segments of the initial conical wavefront arriving at the surface at different angles (in geometric acoustics terms, this manifests as ray bending). As a result of these combined factors, waves observed at various distances from the projection of the aircraft's trajectory on the ground traverse different lengths within the turbulent layer inhomogeneities, exhibiting varying degrees of random waveform distortion.

To identify the key physical aspects of the discussed problem, it is advisable to consider it in a simplified formulation. First, to simplify modeling in terms of initial and boundary conditions, the initial wavefront can be assumed planar, and a two-dimensional geometry can be selected due to computational resource limitations. Thus, calculations are conducted in a rectangular domain, with one side of the rectangle aligned along the evolution coordinate of the one-way wave equation. Second, turbulence can be considered homogeneous and isotropic. Then, a single spatial power spectrum of the random field with a few parameters can be used to specify its properties. Third, since fluctuations in sound speed, even in strong atmospheric turbulence, are relatively small (usually no more than 0.5–1.0%), diffraction angles are small, and thus the nonlinear parabolic KZK equation can be employed. A specialized version of the KZK equation was derived and justified for a moving medium [90] and subsequently employed in numerical modeling [91, 92]:

$$\frac{\partial}{\partial\tau}\left[\frac{\partial p}{\partial z}-\frac{\beta}{\rho_0 c_0^3}p\frac{\partial p}{\partial\tau}-\frac{\delta}{2c_0^3}\frac{\partial^2 p}{\partial\tau^2}\right.$$
$$\left.-\frac{\Delta c+u_z}{c_0^2}\frac{\partial p}{\partial\tau}+\frac{1}{c_0}\left(\mathbf{u}_\perp\cdot\nabla_\perp p\right)\right]=\frac{c_0}{2}\Delta_\perp p. \quad (26)$$

Here, in addition to the notation used in Eqs. (11) and (12), $\Delta c = c - c_0$ denotes scalar sound speed inhomogeneities caused, for instance, by air temperature fluctuations; u_z is the longitudinal component of the medium velocity vector $\mathbf{u}$ (wind); $\mathbf{u}_\perp$ is the transverse component of this vector; $\nabla_\perp$ is the gradient over transverse coordinates; and $\Delta_\perp$ is the Laplacian over transverse coordinates.

Since the wave field in this problem is impulsive, the numerical model was constructed using numerical schemes formulated in the time domain. This removes the necessity of performing Fourier transforms to convert to and from the spectral representation of the pressure field. As initial conditions, a planar N-wave is usually set within a sufficiently long temporal window, ensuring the waveform remains within this window in the moving coordinate system despite sound-speed fluctuations. Other initial waveforms, such as those corresponding to a "low-boom" design, can also be used. For collecting statistical data, sufficiently long transverse realizations of turbulent fields of medium velocity or temperature are generated, then converted into sound speed and acoustic refractive index. Realizations are generated using the random Fourier modes method [91]. Typically, the von Kármán turbulence spectrum consistent with experimental data is employed [93, 94]. For example, in two-dimensional modeling, the von Kármán energy spectrum of kinematic turbulence is described by the expression

$$E\left(\mathbf{K}\right)=\frac{55}{18}\frac{\langle u_z^2\rangle}{c_0^2 L_0^{5/3}}\frac{K^3\exp\left(-K^2/K_m^2\right)}{\left(K^2+K_0^2\right)^{17/6}}. \quad (27)$$

Here, $\mathbf{K}=(K_x,K_z)$ is the spatial spectrum vector, $\langle u_z^2\rangle$ is the mean square of fluctuations of the longitudinal velocity component u_z, $K_m = 5.92/l_0$, and $K_0 = 1/L_0$. The spectrum is characterized by an outer scale L_0 associated with the size of the largest vortices, an inner scale l_0 below which vortices dissipate, and an intensity represented by the root-mean-square fluctuation level of the refractive index for the

longitudinal component, $\sqrt{\langle u_z^2 \rangle}/c_0$. The amplitude of medium-parameter fluctuations near the transverse boundaries of the computational domain is typically smoothed to zero to reduce spurious reflections. In this case, the type of transverse boundary conditions is less important, so the simplest conditions, such as a rigid wall, are chosen. Periodic boundary conditions may also be used. After computing the acoustic field at each step along the evolution coordinate, histograms of various impulse characteristics were constructed and subsequently processed.

Initially, the physical parameters of the numerical model were matched to laboratory experiments conducted in collaboration with colleagues from the École Centrale de Lyon (France) to study the propagation of N-waves in a turbulent layer under well-controlled conditions [93, 94]. In these experiments, spherical N-waves of short duration (30–40 μs) and high amplitude (up to 1500 Pa at a distance of 15 cm from the source) were generated by high-voltage spark discharge [95]. For pulses with such temporal scales, absorption mainly occurs due to thermoviscous effects, so the shock front width, classically defined as the duration between threshold levels at 10% and 90% of the peak positive pressure $p_{\max}$ in the waveform, can be calculated using Taylor's expression $\tau_{\text{sh}} = 4.4\delta\rho_0/(\beta p_{\max})$. Relaxation effects related to the excitation of vibrational degrees of freedom of N_2 and O_2 molecules are also important, causing additional absorption and some asymmetry of the waveform due to dispersion [95]. In the experiments, turbulence was generated either at the exit of a powerful air jet from a nozzle (kinematic turbulence) [93] or in convective flows over a specialized heating grid (thermal turbulence) [94]. Turbulence spectra were measured using hot-wire anemometry or resistance thermometry signals and verified for conformity with the von Kármán model of homogeneous isotropic turbulence. The outer scale of turbulence was about 15–20 cm, and the propagation distance in the layer with inhomogeneities reached 2 m. The turbulence intensity, in terms of root-mean-square fluctuations of acoustic refractive index, did not exceed 1%, both in kinematic and thermal turbulence. Since the wave processes studied occur similarly in real atmospheric scales, illustrative materials (Fig. 3 and Fig. 4) are presented based on modeling data for a full-scale N-wave.

Results of numerical modeling of the N-wave propagation process generally showed good agreement with the data from laboratory experiments. To illustrate the underlying physical phenomena, it is convenient to consider the following statistical characteristics of the positive peak pressure (hereinafter referred to as amplitude for brevity), normalized by values obtained in homogeneous air: mean and standard deviation to evaluate the general level of fluctuations, as well as cumulative probabilities of exceeding a certain threshold to track caustic formation. Since under the given physical parameters the amplitude at caustics typically exceeds the nominal level by no more than several times, the probability of twofold exceeding the nominal amplitude was considered [92]. In the literature, in addition to amplitude statistics, it is common to analyze the statistics of shock front width, as it closely relates to perceived noise levels. However, with strong waveform distortions, the usual definition of shock front width using thresholds of 10 and 90% of amplitude can yield significantly inflated results. Additionally, the pressure drop often occurs not at a single front but rather through a series of multiple fronts with random pressure differences. Therefore, in the numerical experiment, instead of front width, its steepness, defined by the peak of the waveform derivative, was calculated [92]. In this approach, the steepest section of the waveform is automatically identified and considered the "shock" front. For steepness normalized by corresponding values in a homogeneous medium, a set of statistical data analogous to that computed for amplitude was also considered. Statistical data were analyzed as functions of the distance traveled by the wave. It should be noted here that numerical modeling has a significant advantage over experiments when analyzing impulse time characteristics because, due to measurement device limitations (high-frequency cutoff of microphones), shock fronts were smoothed, resulting in measured widths several times or even an order of magnitude larger than actual values [95].

As the wave propagates through the turbulent layer, the initially planar wavefront begins to bend randomly due to sound speed inhomogeneities of different signs, causing focusing and defocusing of waves. This process develops gradually, involving progressively larger-scale inhomogeneities until, at some distance, the strongest caustics with maximum wave amplitude amplification form, caused by large-scale inhomogeneities in the turbulence spectrum (Fig. 3). Caustics are elongated structures, and their amplitude remains high at distances several times greater than the distance at which the first strong focusing occurs. However, defocusing regions with low amplitude noticeably expand transversely. Waveforms exhibit significant diversity; for example, in caustic regions, they adopt a high-amplitude form called a U-wave, whereas waveforms in defocusing regions feature blurred shock fronts and reduced amplitude (Fig. 4). In statistical data, these processes manifest as an initial linear growth of standard deviation in amplitude and front steepness. The standard deviation for both values reaches a maximum at the

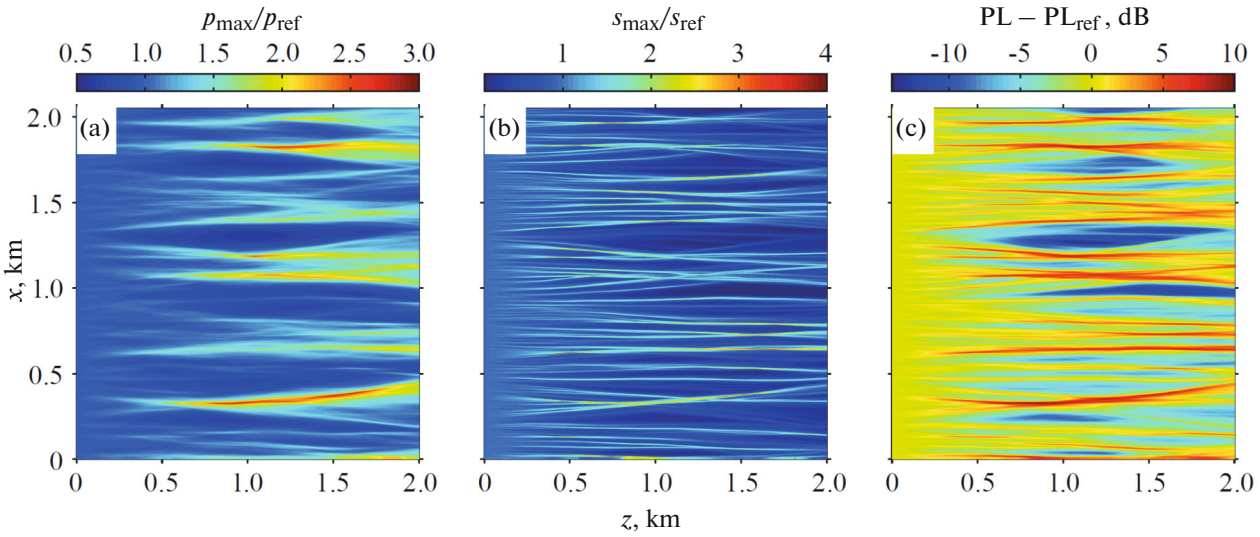

Fig. 3. Examples of random realizations of N-wave parameters, normalized to their respective nominal levels, obtained from numerical modeling of nonlinear pulse propagation in a full-scale turbulent atmosphere: (a) peak positive pressure, (b) shock front steepness, (c) impulse noise metric perceived loudness Mark VII.

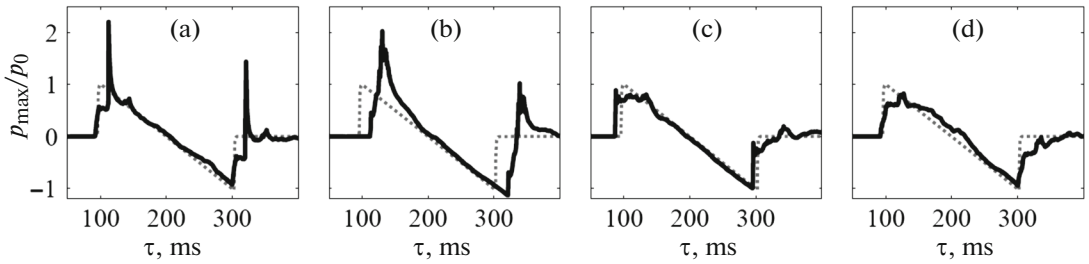

Fig. 4. Examples of random waveform distortions during the propagation of an initial N-wave with an amplitude of $p_0 = 20$ Pa (shown by a dashed line) in a full-scale turbulent atmosphere over a distance of 2 km: (a, b) in the caustic region with pressure amplification; (c, d) outside the caustic region with shock front blurring effects.

distance of the first caustic formation and subsequently decreases slowly. At the same time, fluctuations in front steepness are several times greater than amplitude fluctuations. Cumulative probability curves also exhibit a maximum corresponding to the distance where the first caustics form.

Numerical modeling conveniently allows qualitative and quantitative analysis by varying input parameters within certain ranges or even by switching off specific physical effects. Here, the influence of nonlinear effects was primarily studied by performing calculations with different amplitudes of the initial N-wave (from 50 to 400 Pa), as well as with the nonlinear operator disabled (linear problem). It was shown that the degree of nonlinear effects has a relatively weak influence on the curves of mean and standard deviation of amplitude. Significant differences can be found on cumulative probability curves, where differences in maximum probability can reach up to two times (from 2 to 4% for twice exceeding the nominal amplitude level). This is explained by enhanced focusing effects in random caustics due to the greater steepness of the front at higher initial wave amplitudes [91]. For front steepness statistics, linear model results show that the mean front steepness decreases quite rapidly, and the cumulative probability of doubling the steepness is very small, less than 1%. Thus, due to scattering by inhomogeneities of various scales, the initially steep front rapidly smooths out without the support of nonlinear effects. In the presence of nonlinear effects, the level of steepness fluctuations strongly depends on their intensity, and the maximum standard deviation and cumulative probability differ several times depending on the initial N-wave amplitude. It can also be observed that the stronger the nonlinear effects, the slower the intensity of amplitude and front steepness fluctuations decreases with distance. Thus, under laboratory modeling conditions, nonlinear effects play a crucial role in maintaining a sufficiently steep wavefront and preventing its smoothing even over large distances in randomly inhomogeneous media.

It is also interesting to note that although mod-

eling was carried out in two-dimensional geometry while the experimental setup was three-dimensional, statistically, the theoretical and experimental results turned out to be quite close [91, 93]. This is explained by the fact that, as subsequently shown by other researchers using three-dimensional modeling [96], differences between two-dimensional and three-dimensional models primarily appear in the high-amplitude "tails" of distributions, corresponding to low probabilities.

The developed numerical model can be relatively easily adapted to analyze N-wave propagation at real scales, since nearly all physical processes involved are analogous. The duration of a real N-wave typically ranges from 100 to 300 ms, so due to the relatively low frequencies of such impulses, thermoviscous absorption gives way to relaxation processes. In work [97], a similar study was conducted based on the above-described model, analyzing noise metrics alongside previously mentioned nonlinear pulse characteristics (amplitude and front steepness). Such metrics are used to normalize noise levels from supersonic aircraft in relevant regulatory documents. Here, the standard PL (perceived loudness) Mark VII metric was considered, as it correlates well with subjective noise levels and is almost universally calculated in studies on this topic. Similar to the analysis at laboratory scales, numerical modeling to assess nonlinear effects varied the amplitude of the initial N-wave from 10 to 40 Pa, corresponding to realistic pressure levels of supersonic aircraft of various designs. It was demonstrated that, qualitatively, the statistics of amplitude and front steepness in real-scale modeling behave similarly to those obtained from laboratory-scale experiments. One qualitative difference, caused by the lower absorption levels at real scales compared to laboratory experiments, was observed in the mean amplitude, which instead of decreasing, showed a slight increase (from +10 to +30% relative to nominal values) after passing the distance where strong caustics formed. According to the modeling results, the mean value of the PL Mark VII metric in a turbulent medium slightly decreases by 1–2 dB compared to its nominal level in homogeneous air. It was shown that, at low and moderate initial N-wave amplitudes (10 and 20 Pa), statistical results for the normalized noise metric are nearly identical. Under these conditions, the standard deviation peaks at 3 dB at the distance of the strongest caustic formation, and the cumulative probability of exceeding the nominal noise level by 6 dB does not exceed 3% at maximum. Increasing the N-wave amplitude to 40 Pa slightly raises both the standard deviation (up to 4 dB) and the cumulative probability for the noise metric (up to 4%). At this amplitude level, fluctuations in amplitude and front steepness significantly increase as well. These phenomena are apparently related to the growth of the high-frequency part of the impulse spectrum due to reduced shock front width. As a result, the high-frequency edge of the wave spectrum shifts toward the most sensitive frequency range of human hearing, increasing loudness in regions of random focusing, thus significantly affecting fluctuations of the noise metric.

Thus, numerical modeling using the KZK equation in the problem of impulsive wave propagation with steep fronts in a randomly inhomogeneous medium enabled the identification of several important quantitative and qualitative features of the acoustic field of a nonlinear wave and its statistical characteristics. The quantitative data obtained from numerical modeling methods were confirmed by laboratory experiment results, as well as by a comprehensive collection of literature data gathered from field tests involving supersonic aircraft overflights [98].

3.2. Registration of Nonlinear Pulses in Air by Optical Methods

As mentioned earlier, the main challenge in aeroacoustic measurements in laboratory experiments was that condenser microphones used for recording pulsed signals had a limited frequency bandwidth [95]. As a result of filtering, the shock fronts of N-waves were significantly smoothed, and the shock front width was overestimated by almost an order of magnitude. Additionally, the measured signal contained oscillations caused by microphone membrane resonances at frequencies around 150 kHz. Therefore, in the course of laboratory modeling experiments, a separate research direction was developed for optical registration of weak shock pulses from a spark source. Numerical modeling of spherical N-wave propagation using a modified Burgers equation also played a significant role here. Thus, specifying an initial waveform at a certain distance near the source allowed obtaining waveforms at any other distances greater than the initial one. As a result, it became possible to correlate a series of N-waveform measurements at different distances from the source with theoretical predictions.

In the simple shadow method, the region through which the spherical N-wave propagates was illuminated by a parallel beam of white light from a short spark flash, and the resulting shadow pattern was recorded [99]. This method is sensitive to sharp variations in the optical refractive index at shock fronts, and it enabled measurement of the front width, which closely matched values obtained from Burgers equation modeling for the spherical N-wave. To reconstruct the complete acoustic waveform, the Schlieren

method was applied, which generally provided good results, except for the blurring of the shock front in the image due to the insufficient response time of the digital camera [100]. The best data were obtained using a setup based on a Mach–Zehnder interferometer operating in an infinite fringe width mode [101]. The temporal resolution was determined by the width of the laser beam at the point of contact with the spherical wavefront and was 0.4 μs, which is at least six times superior to the capabilities of commercial condenser microphones (e.g., B&K type 4138, 1/8 inch). Numerical modeling of the Burgers equation for spherical waves was used to estimate the error in the waveform reconstruction procedure based on the optical signal integrated along the laser beam passing through a radially symmetric acoustic pressure distribution. A separate numerical algorithm, which was part of the waveform reconstruction procedure, was implemented to perform the inverse Abel transform [100].

The quality of the reconstructed experimental nonlinear waveform was so high that optical measurement results from the Mach–Zehnder interferometer were used as a reference in the procedure for determining the amplitude and phase–frequency response of acoustic microphones. Initially, standard microphones (B&K type 4138, 1/8 inch) were calibrated [101], and later, the optical setup was used to test prototypes of advanced high-frequency microphones with a theoretical bandwidth of up to 1 MHz, fabricated using MEMS (microelectromechanical systems) technology [102].

Subsequently, the interferometer was used for experimental studies of the reflection process of a weak shock wave generated by a spark source in model experiments, under conditions leading to the formation of a "Mach stem" [103]. In this study, waveforms were measured at different heights above a flat surface, and the reflection pattern was mapped at several distances from the spark source. Based on these data, the height of the "Mach stem" was determined, and its evolution was tracked as the wave traveled further along the surface. Experimental data from optical measurements of irregular reflection of a nonlinear wave were compared with direct numerical simulations of compressible fluid equations and were found to be in good agreement with theory [104, 105].

4. PARAMETRIC PROCESSES IN ULTRASONIC BEAMS

The numerical modeling methods for one-way nonlinear wave equations developed in the laboratory were used to study a classical problem in nonlinear acoustics related to the interaction of high-amplitude waves of different frequencies. In the early 1960s, the concept of an end-fire parametric antenna was independently proposed by P. Westervelt in the USA [5] and by V.A. Zverev and A.I. Kalachev in the USSR [106]. During the nonlinear interaction of two high-intensity high-frequency pump waves in a medium, a cascading process of generating multiple spectral components occurs. At a certain distance from the source, due to frequency-dependent absorption in the medium, the pump waves significantly attenuate, and only the low-frequency component—the difference-frequency wave (DFW)—continues to propagating. The advantages of this method of low-frequency radiation generation include a narrow high directivity pattern within a few degrees with no sidelobes, as well as the ability to use high-frequency transducers that are small compared to the wavelength of the low-frequency radiation [107]. The main drawback of the parametric generation of difference-frequency radiation is its relatively low efficiency since the energy of the pump waves mostly propagates upward in the spectrum, where it is absorbed, while only a small fraction is transferred downward, i.e., into the DFW.

Nevertheless, interest in studying the characteristics of nonlinear interactions in parametric transducers remains strong. For instance, low-frequency parametric transducers are used in hydroacoustic applications for seabed profiling, long-range ocean research, and underwater communication [108]; in generating highly directional sound beams in air for active noise control systems and targeted communication with users in libraries and museums [109]; as well as in medical applications, such as ultrasound imaging at the difference frequency [110].

In the theoretical description of difference-frequency wave generation and propagation, the one-way Westervelt equation [5] or the parabolic Khokhlov–Zabolotskaya–Kuznetsov equation [4] is typically used under the assumption that the diffraction divergence of both the high-frequency pump waves and the generated low-frequency component is less than 15° [20]. Modern studies of parametric interactions rely on numerical modeling, as analytical solutions have only been obtained using various approximations in describing nonlinear and diffraction effects: in the quasi-linear approximation of pump wave interaction [5, 107], with an approximate description of discontinuities in the nonlinear waveform [111], and considering simplified boundary conditions at the transducer [5, 107]. However, even the existing numerical algorithms based on the KZK or Westervelt equations [112–116] were developed for the quasi-linear approach and/or axial beam symmetry, or for relatively small pump-to-difference frequency ratios and moderate nonlinear propagation conditions [117].

A fully nonlinear three-dimensional algorithm for solving the problem of difference-frequency wave parametric generation was recently developed in the LIMU laboratory [118], designed for sources with arbitrary pump-to-difference frequency ratios and varying degrees of nonlinear effects, as well as for realistic transducer conditions with precise diffraction modeling in highly directional beams for both pump waves and the difference-frequency wave [119]. The KZK equation was numerically solved in the spectral domain using the spectrum filtering method [120], which was validated based on solutions of the Burgers equation for a planar nonlinear problem.

The essence of the spectrum filtering method (Fig. 5a) is based on its specific features in two-frequency interaction and is as follows. As previously mentioned in the description of one-way equation solution algorithms for medical ultrasound problems, to correctly account for nonlinear interactions, particularly in the formation of shock fronts, a numerical algorithm must use approximately a thousand or at least several hundred harmonics. In this case, we refer to the harmonics of high-frequency pump waves. Considering the ratio between the difference frequency and the pump wave frequencies, which can reach several tens, the required number of harmonics increases to tens of thousands. Such a large number of spectral components makes three-dimensional modeling practically infeasible due to both the significant memory required to store data arrays and the long computation time. However, a detailed examination of the nonlinear wave spectra in two-frequency pumping reveals that most spectral components have low amplitudes and contribute minimally to DFW generation. This enables optimization of the spectral algorithm for solving the KZK equation by selecting a limited subset of harmonics from the full discrete spectrum based on a threshold criterion. That is, if the amplitude of a given harmonic exceeds a set threshold, it is retained in the algorithm; otherwise, it is discarded. The model also introduced artificial absorption, which allowed for a faster reduction of the highest harmonic amplitudes while having minimal impact on the low-frequency part of the spectrum. According to the proposed method, a set of fifty high-amplitude spectral components was identified at a certain distance from the source as contributing the most to low-frequency radiation generation. The error introduced by spectral truncation was evaluated by comparing numerical solutions of the Burgers equation for a planar wave with a biharmonic initial waveform, calculated using both the full-spectrum and optimized algorithms. As a result, it was found that the error does not exceed 2% at all considered distances, which span several characteristic nonlinear lengths [120]. Alternative criteria for selecting the harmonic set for spectrum filtering were investigated; however, they did not yield better results [121].

In the three-dimensional problem, spectrum filtering significantly (by orders of magnitude) reduced the computational load, making it feasible to conduct simulations within a reasonable time frame (several days for a single calculation). In the operator splitting method for the KZK equation, reducing the number of harmonics proportionally decreases the computation time for diffraction and absorption operators. The spectrum filtering method proved particularly advantageous when optimizing the spectral algorithm for the nonlinearity operator, as the number of computational operations in this algorithm scales with the square of the number of harmonics (9). Unfortunately, optimizing calculations for pulsed signals, which have an inherently broad spectrum, is not feasible using this method, necessitating the search for alternative approaches.

The developed algorithm was used to model an end-fire parametric antenna (Fig. 5b) based on a multielement two-channel underwater pump wave transducer of elliptical shape with an axis ratio of 1.69 [122]. The frequency of one of the pump waves was fixed at 150 kHz, while the second component's frequency varied between 135 and 145 kHz, corresponding to DFW frequencies from 5 to 15 kHz. Numerical modeling refined many effects that had previously been studied mainly qualitatively using approximate analytical models [107]. For example, analytical solutions suggest that in a plane wave, the DFW amplitude increases linearly with frequency until the absorption of pump waves becomes significant. In DFW beam generation, the amplitude growth along the axis exceeds linear behavior because, at higher DFW frequencies, diffraction divergence is less pronounced. An effect of field symmetrization for DFW generated by pump waves from an ellipsoidal transducer was demonstrated. For instance, while the beamwidths of the pump waves for this transducer differ by a factor of 1.6 along two mutually perpendicular directions in the transverse plane, this ratio decreases to 1.14 for the DFW. Additionally, beamwidth of DFW nearly doubles when transitioning from a quasi-linear pump wave interaction regime to strongly nonlinear conditions. This is explained by the fact that in such cases, difference-frequency wave generation primarily occurs in the near field of the pump wave beam. Consequently, the DFW beam size is small, leading to a stronger manifestation of diffraction divergence effects.

The efficiency of DFW generation was investigated based on two criteria: the ratio of the DFW amplitude on the beam axis to the amplitude of the pump waves at the transducer (relative amplitude), and the ratio of the total acoustic power of the DFW beam

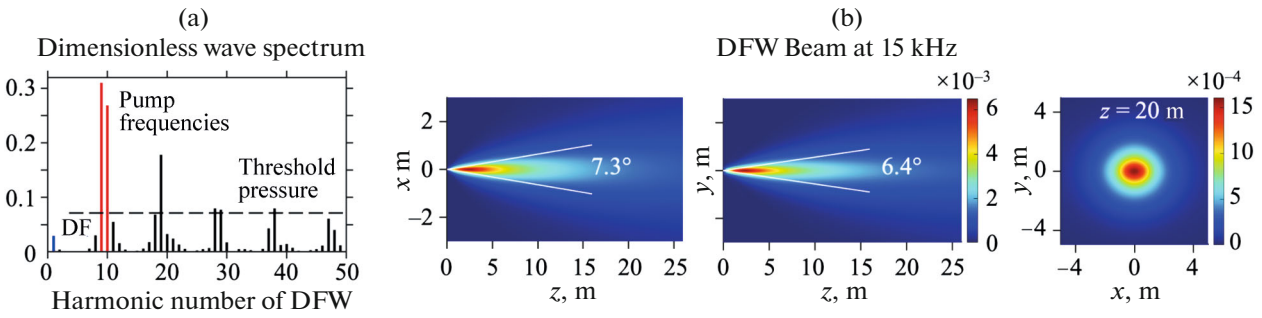

Fig. 5. Numerical modeling of parametric radiation based on the KZK equation in the spectral representation of the pressure field: (a) illustration of the spectral filtering method based on a threshold, (b) two-dimensional longitudinal (x, z) and (y, z) and transverse (x, y) distributions of the pressure field of the difference-frequency wave at 15 kHz.

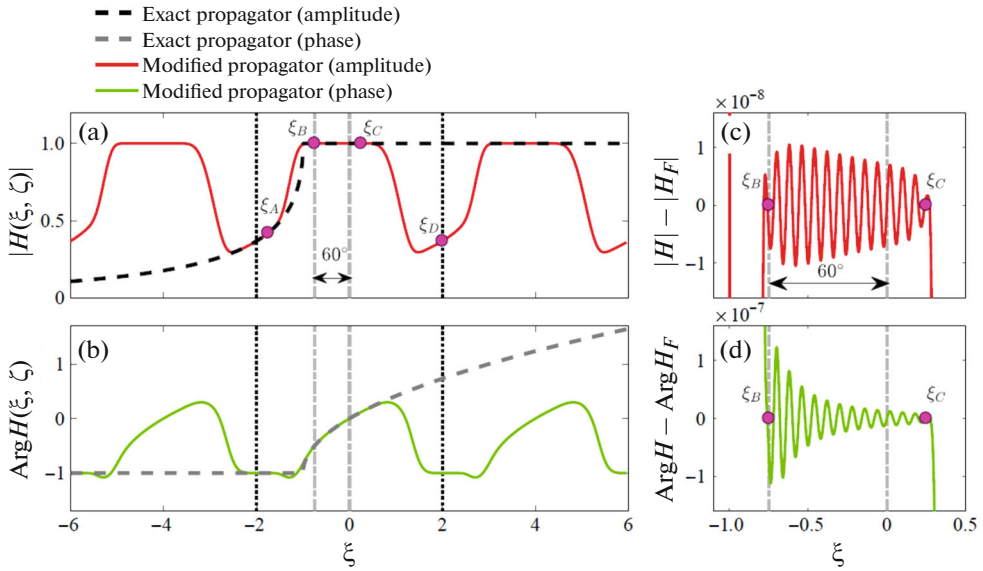

Fig. 6. Method for constructing a wide-angle one-way wave model based on the Fourier operator series: (a, b) amplitude and phase of the exact (dashed line) and periodically extended modified propagator (solid line) for the Fourier expansion in a window of width $\xi_L = 4$ for the model with $\theta_{\max} = 60^\circ$ at $|\zeta| = 1$; (c, d) approximation error in amplitude and phase when expanding the modified propagator into a finite Fourier series with the number of harmonics $2N = 100$. The vertical dash-dotted lines indicate the angular range of propagating waves represented in the model. The vertical dashed lines mark the boundaries of one period of the modified propagator.

to the total power of the pump wave beams. It was shown that the relative amplitude initially increases linearly with the pump wave amplitude, in accordance with the quasi-linear model, and then, with a further increase in pump wave intensity, reaches saturation, which is consistent with analytical estimates [111]. Saturation occurs due to a significant increase in nonlinear absorption as shock fronts form. In absolute units of acoustic pressure, saturation on the beam axis corresponds to the continued linear growth of the DFW amplitude. The relative power of the DFW beam continues to increase without saturation because, as the pump wave amplitude grows, the periphery of the beam contributes to the generation. For a DFW at 15 kHz, the power ratio in the strongly nonlinear regime was 0.05%.

Thus, a series of studies demonstrated that the fully nonlinear three-dimensional approach based on the KZK equation allows for a detailed investigation of the quantitative characteristics of the parametric generation of low-frequency radiation and enables the determination of optimal pump wave radiation parameters to maximize output power at the difference frequency while maintaining the desired directivity of the low-frequency beam.

5. WIDE-ANGLE PARABOLIC EQUATION METHODS IN NUMERICAL MODELING OF WAVES IN INHOMOGENEOUS MEDIA BASED ON ONE-WAY EQUATIONS

5.1. Main Approaches to Constructing Wide-Angle Parabolic Models

In the previous sections of this review, apart from aeroacoustic problems, the focus was primarily on

the application of one-way numerical models for studying nonlinear wave processes in homogeneous media. However, in many practically important cases, significant interest lies in studying the influence of inhomogeneities on wave propagation, as they can cause substantial changes in the spatial distribution of the wave field compared to a homogeneous medium [123]. For example, in medical applications of high-intensity ultrasound, beam focusing in the therapeutic region occurs through layers of soft biological tissues, which, from an acoustic standpoint, constitute a weakly inhomogeneous medium [124]. Inhomogeneities in the speed of sound introduce aberrations that degrade beam focusing quality, manifesting as a decrease in amplitude at the focus and a shift in its position [125]. The distortion of the acoustic field makes therapeutic exposure unpredictable and, in some cases, may even prevent it from being performed if the required wave characteristics at the focus are not achieved [126]. Therefore, these wave phenomena require detailed investigation using appropriate theoretical models that account for inhomogeneities.

One-way wave models, with certain assumptions, can be extended to inhomogeneous media, where the speed of sound, medium density, and other parameters (such as nonlinearity and absorption coefficients) are functions of spatial coordinates [127]. It should be noted that when the initial wave propagates predominantly in one direction, the presence of inhomogeneities not only distorts the incident wave but also generates reflected waves traveling in the opposite direction. Strictly speaking, in this case, one-way models no longer fully describe the wave process. However, if the inhomogeneities are sufficiently weak and smooth, the amplitude of the reflected waves remains small and can be neglected. In this case, applying one-way models to describe wave propagation in inhomogeneous media is justified and does not introduce significant errors. If the Westervelt equation in an inhomogeneous medium is taken as the basis, the main difficulty in solving it arises from the diffraction term, which is equivalent to the conventional wave equation in the time domain or the Helmholtz equation in the frequency domain for the pressure field. Therefore, to construct a one-way model, wide-angle parabolic approximation methods can be used, which are frequently applied in a broad range of problems involving one-way wave propagation in inhomogeneous media in various fields of acoustics [128, 129], geophysics [11], as well as in radio physics [130] and optics [131].

If the z-axis is chosen as the preferred direction of wave propagation, the Helmholtz equation for the complex amplitude of the pressure field p is typically written in the operator form [132]:

$$\frac{\partial^2 p}{\partial z^2} + k_0^2 \widehat{Q}^2 p = 0, \tag{28}$$

where the operator $\widehat{Q}^2 = 1 + \widehat{L}$ is defined, and $\widehat{L}$ is a differential operator containing the Laplacian over the transverse coordinates x and y, as well as functions describing inhomogeneities in the speed of sound c and medium density ρ [133]:

$$\widehat{L} = n_a^2 - 1 + \frac{\rho}{k_0^2}\left(\frac{\partial}{\partial x}\left(\frac{1}{\rho}\frac{\partial}{\partial x}\right) + \frac{\partial}{\partial y}\left(\frac{1}{\rho}\frac{\partial}{\partial y}\right)\right). \tag{29}$$

Here, $k_0 = \omega_0/c_0$ is the reference wavenumber corresponding to the reference speed of sound c_0, and $n_a = c_0/c$ is the acoustic refractive index in a medium with a speed of sound distribution $c(x, y, z)$. The case of smooth variations in inhomogeneities along the z-axis is considered here, so this dependence can be locally neglected. In the general case, to account for smooth longitudinal variations in the medium's properties, a special normalization factor is introduced, which depends on the medium parameters and links the pressure to a new variable for which the one-way equation is derived [134].

The normal mode method is often used to describe one-way wave propagation [135]. According to this method, the pressure field in the Helmholtz equation (28) can be represented as a superposition of normal modes

$$p = \sum_m p_m(z)\,\psi_m(x, y), \tag{30}$$

where the functions $p_m(z)$ are proportional to $\exp(ik_m z)$, and the normal modes ψ_m and eigenvalues k_m^2 satisfy the equation:

$$k_0^2\left(n_a^2 - 1\right)\psi_m + \rho\left(\frac{\partial}{\partial x}\left(\frac{1}{\rho}\frac{\partial}{\partial x}\right) + \frac{\partial}{\partial y}\left(\frac{1}{\rho}\frac{\partial}{\partial y}\right)\right)\psi_m = k_m^2\psi_m. \tag{31}$$

Furthermore, the modes satisfy the orthogonality condition

$$\iint_D \rho^{-1}\psi_m(x, y)\,\psi_n(x, y)\,dxdy = \delta_{mn}, \tag{32}$$

where D is the domain in the transverse plane (x, y) where the problem is considered, δ_{mn} is the Kronecker delta, and $m > 0$, $n > 0$ are the mode indices. In compact notation, using the classical differential operator $k_0^2\widehat{Q}^2$, the eigenfunction and eigenvalue problem is represented as

$$k_0^2\widehat{Q}^2\psi_m = k_m^2\psi_m. \tag{33}$$

Applying the operator $k_0^2\widehat{Q}^2$ to the function ψ_m an integer number of times $J > 0$, we obtain

$$\left(k_0^2\widehat{Q}^2\right)^J \psi_m = \left(k_m^2\right)^J \psi_m. \tag{34}$$

Thus, for some function $f(X)$, which can be expanded into a convergent Taylor series, we can write

$$f\left(k_0^2\widehat{Q}^2\right)\psi_m = f\left(k_m^2\right)\psi_m. \tag{35}$$

In the particular case of the function $f(X) = \sqrt{X}$ for $X > 0$ and $X < 2$, we obtain

$$k_0\widehat{Q}\psi_m = k_m\psi_m, \tag{36}$$

where $\widehat{Q} = \sqrt{1+\widehat{L}}$ is a pseudodifferential operator. In general, the operator $k_0^2\widehat{Q}^2$ can have negative eigenvalues, which correspond to nonpropagating waves (where k_m is imaginary). In this case, the branch of the square root function is chosen such that it ensures attenuation of these waves with distance.

Using the modal representation of the field, a one-way equation can be derived. For example, if we consider a single mth mode, the field for it is

$$p = e^{ik_m z}\psi_m(x,y). \tag{37}$$

Differentiating with respect to z gives:

$$\frac{\partial p}{\partial z} = ik_m e^{ik_m z}\psi_m(x,y). \tag{38}$$

Using the definition of the operator $\widehat{Q}$ (36), the right-hand side of this equation can be rewritten, yielding a one-way pseudodifferential equation for a single mode:

$$\frac{\partial p}{\partial z} = ik_0\widehat{Q}p. \tag{39}$$

Since each solution of the original Eq. (28) can be expressed as a superposition of modes, the obtained equation is also valid for a wave that is a solution and propagates in the direction of $z > 0$. In the theory of wide-angle parabolic equations, further derivations are typically carried out using a more compact operator formalism based on the modal representation of the pressure field.

Thus, the Helmholtz equation in operator form can be factorized into two factors:

$$\left(\frac{\partial}{\partial z} + ik_0\sqrt{1+\widehat{L}}\right)\left(\frac{\partial}{\partial z} - ik_0\sqrt{1+\widehat{L}}\right)p = 0. \tag{40}$$

Here, in the right-hand side, in a smoothly inhomogeneous medium, the commutator of the operator $\partial/\partial z$ and the pseudodifferential operator $\widehat{Q} = \sqrt{1+\widehat{L}}$ is typically neglected. This results in two equations, one corresponding to waves propagating in the direction of $z > 0$, and the other in the direction of $z < 0$ [136]. Selecting only one propagation direction for waves toward positive z, the one-way evolution equation for the slowly varying pressure envelope $\varphi = p\exp(-ik_0 z)$ is written as [137]

$$\frac{\partial\varphi}{\partial z} = ik_0\left(\sqrt{1+\widehat{L}} - 1\right)\varphi. \tag{41}$$

Due to the presence of the pseudodifferential operator $\widehat{Q} = \sqrt{1+\widehat{L}}$ on the right-hand side, solving this equation is quite difficult, as it would require finding all modes and their corresponding eigenvalues, which is generally a computationally demanding task. Therefore, in practical numerical modeling, various approximations of the operator $\widehat{Q} \approx \widehat{Q}_a$ are used to avoid solving the eigenvalue problem and to employ other, less computationally expensive solution methods [138]. From the perspective of modal decomposition, applying an approximate operator $\widehat{Q}_a$ implies the following. From the perspective of modal decomposition, applying an approximate operator $\widehat{Q}_a$ implies the following:

$$\widehat{L}\psi_m = \frac{k_m^2 - k_0^2}{k_0^2}\psi_m, \tag{42}$$

according to which the eigenvalue of the operator $\widehat{L}$ is $\xi_m = \left(k_m^2 - k_0^2\right)/k_0^2$. Using the same reasoning as for the operator $k_0^2\widehat{Q}^2$, it can be shown that for a certain function $f(X)$, the following holds:

$$f\left(\widehat{L}\right)\psi_m = f\left(\frac{k_m^2 - k_0^2}{k_0^2}\right)\psi_m. \tag{43}$$

Therefore, replacing the exact operator $\widehat{Q} = \sqrt{1+\widehat{L}}$ with its approximation $\widehat{Q}_a(L)$ in Eq. (39) and substituting the solution in the form of a single mode $p = e^{i\tilde{k}_m z}\psi_m$, we obtain

$$\tilde{k}_m = k_0 Q_a\left(\frac{k_m^2 - k_0^2}{k_0^2}\right). \tag{44}$$

Here, $Q_a(\xi)$ is an approximating function for $\sqrt{1+\xi}$, and $\tilde{k}_m$ is the approximate value of the wavenumber. Thus, in the solution of the approximate one-way equation, the modes ψ_m remain unchanged, while the exact wavenumbers k_m are replaced by their approximate values $\tilde{k}_m$, corresponding to a given approximating function.

For example, if we use the linear expansion $\sqrt{1+\widehat{L}} \approx 1 + \widehat{L}/2$, we obtain the standard parabolic diffraction equation [139]:

$$\frac{\partial\varphi}{\partial z} = \frac{ik_0}{2}\widehat{L}\varphi, \tag{45}$$

which was previously discussed for the case of a homogeneous medium ($n_a = 1$, $\rho = \text{const}$). Expanding the operator $\widehat{Q}$ into a Taylor series to higher orders in $\widehat{L}$ to improve the approximation accuracy and extend the angular range of the approximate equation turns out to be ineffective [140], and Padé approximations in the form of a product or sum of rational functions are mainly used [141]:

$$\widehat{Q} \approx \prod_{l=1}^{N_l} \frac{1+\mu_l \widehat{L}}{1+\nu_l \widehat{L}} = 1 + \sum_{l=1}^{N_l} \frac{\alpha_l \widehat{L}}{1+\beta_l \widehat{L}}, \tag{46}$$

where the integer $N_l > 0$ defines the order of approximation $2N_l$, and (μ_l, ν_l) and (α_l, β_l), $l = 1 \dots N_l$ are the corresponding sets of coefficients that are determined in various ways [142]. For example, for order $N_l = 1$, one of the first wide-angle equations is known [143]:

$$\frac{\partial \varphi}{\partial z} = \frac{ik_0}{2} \frac{\widehat{L}}{1+\widehat{L}/4} \varphi. \tag{47}$$

Next, the one-way equation, similar to how it was done with the standard parabolic equation, can be approximated using the generalized Crank–Nicolson scheme [143]:

$$\left(1 - \frac{\zeta}{2}\left(\widehat{Q} - 1\right)\right) \varphi^{m+1} = \left(1 + \frac{\zeta}{2}\left(\widehat{Q} - 1\right)\right) \varphi^{m}, \tag{48}$$

where φ^{m+1} is the field at the next step $z + \Delta z$, φ^m is the field at the current step z, and $\zeta = ik_0 \Delta z$ is a dimensionless complex parameter, whose magnitude equals the dimensionless grid step along the z-axis. After substituting a specific Padé approximation of the operator $\widehat{Q}$ into Eq. (48) and further factorizing the operators in the left- and right-hand sides, a series of final equations of the form can be obtained:

$$\left(1 + \tilde{\nu}_l \widehat{L}\right) \tilde{\varphi}^{(l+1)} = \left(1 + \tilde{\mu}_l \widehat{L}\right) \tilde{\varphi}^{(l)} \tag{49}$$

with a new set of coefficients $\tilde{\nu}_l$ and $\tilde{\mu}_l$, which are solved using various numerical methods (finite difference, finite element). Here, $\tilde{\varphi}^{(l)}$ represents intermediate fields in solving a series of N_l equations, initialized by the field φ^m at the current step along z.

A more advanced approach involves using the formal solution of the one-way equation:

$$\varphi^{m+1} = \exp\left[\zeta\left(\sqrt{1+\widehat{L}} - 1\right)\right] \varphi^m, \tag{50}$$

obtained after integrating Eq. (41) with respect to z. In terms of modal representation, this solution takes the form:

$$\varphi^{m+1} = \sum_l a_l \psi_l \exp\left[\zeta\left(k_l/k_0 - 1\right)\right], \tag{51}$$

where a_l are the expansion coefficients of the field φ^m in terms of normal modes ψ_l with corresponding wavenumbers k_l. Previously, this solution was called an operator plane wave, which is a collection of normal modes propagating in one direction [10]. In modern literature, the term propagator operator, or simply propagator, is commonly used:

$$\widehat{H} = \exp\left[\zeta\left(\sqrt{1+\widehat{L}} - 1\right)\right], \tag{52}$$

whose arguments are the pseudodifferential operator $\widehat{Q}$ and the dimensionless parameter ζ. According to (51), the propagation operator $\widehat{H}$ corresponds to a complex-valued function of the eigenvalues ξ of the operator $\widehat{L}$:

$$H(\xi, \zeta) = \exp\left[\zeta\left(\sqrt{1+\xi} - 1\right)\right]. \tag{53}$$

In a homogeneous medium, this exactly corresponds to the propagator of the angular spectrum method for $\xi = -\left(k_x^2 + k_y^2\right)/k_0^2 = -\sin^2\theta$, where θ is the angle at which a plane wave with a wave vector $\left(k_x, k_y, k_z = \sqrt{1 - \left(k_x^2 + k_y^2\right)/k_0^2}\right)$ propagates relative to the z-axis. The graph of the amplitude and phase of the propagator is shown in Figs. 6a and 6b with a dashed line. The interval $-1 < \xi \leqslant 0$ corresponds to propagating waves, while the region $\xi \leqslant -1$ corresponds to evanescent inhomogeneous waves that decay exponentially with increasing z. The region $\xi > 0$ is not involved in a homogeneous medium since here $\xi = 0$ is the maximum eigenvalue corresponding to a plane wave with a wave vector $(0, 0, k_0)$ propagating strictly along the z-axis. However, the region $\xi > 0$ appears in the presence of inhomogeneities with a refractive index $n_a > 1$.

Similarly to the operator $\widehat{Q}$ in Eq. (41), the propagator in the formal solution can be directly replaced by Padé approximations of a given order (N_l, N_l) [29, 144]

$$\varphi^{m+1} = \prod_{l=1}^{N_l} \frac{1+\bar{\mu}_l \widehat{L}}{1+\bar{\nu}_l \widehat{L}} \varphi^m, \tag{54}$$

where the coefficients $\bar{\mu}_l = \bar{\mu}_l(\zeta)$ and $\bar{\nu}_l = \bar{\nu}_l(\zeta)$ are functions of the dimensionless step. This representation is equivalent to an approximation for the function $H(\xi, \zeta)$:

$$H(\xi, \zeta) \approx \prod_{l=1}^{N_l} \frac{1+\bar{\mu}_l \xi}{1+\bar{\nu}_l \xi}. \tag{55}$$

The propagator form obtained from the approximation (54) implies solving equations of the same type (49) as when using the generalized Crank–Nicolson scheme for the one-way equation. Alternatively, instead of Padé approximations in the form of a product, Padé approximations in the form of a sum can be used [7]:

$$\varphi^{m+1} = \varphi^m + \sum_{l=1}^{N_l} \frac{\bar{\alpha}_l \widehat{L}}{1 + \bar{\beta}_l \widehat{L}} \varphi^m, \qquad (56)$$

which leads to the need to solve similar equations $\left(1 + \bar{\beta}_l \widehat{L}\right) \tilde{\varphi}^{(l)} = \bar{\alpha}_l \widehat{L} \varphi^m$, differing from equations of the type (49) only by their right-hand side. A feature of Padé approximations in the form of a sum is the ability to solve N_l equations in parallel, followed by summing the partial solutions $\tilde{\varphi}^{(l)}$.

As mentioned in the first section of the article when describing methods for solving the diffraction operator of the radially symmetric Westervelt equation, the wide-angle parabolic equation method is effective in two-dimensional problems where there is a predominant wave propagation direction and only one transverse coordinate. This is because in a two-dimensional problem, equations of the type (49) are one-dimensional, contain derivatives only along a single transverse coordinate, and therefore are well suited for standard numerical methods. For example, when using a second-order finite difference method, the system of equations for pressure field values at numerical grid nodes forms a tridiagonal matrix and is easily solved by the Thomas algorithm [30, 143]. In the three-dimensional problems discussed in this section, the construction of an efficient numerical scheme is significantly more complex.

Since in three-dimensional problems there are two transverse coordinates (e.g., x and y in a Cartesian coordinate system), the differential operator $\widehat{L}$ consists of the sum of two components

$$\widehat{L} = \widehat{L}_x + \widehat{L}_y, \qquad (57)$$

each of which contains derivatives only with respect to one of these two coordinates. For example, with a symmetric division of refractive index inhomogeneities between $\widehat{L}_x$ and $\widehat{L}_y$, it can be written as

$$\widehat{L}_x = \frac{n_a^2 - 1}{2} + \frac{\rho}{k_0^2} \frac{\partial}{\partial x} \left(\frac{1}{\rho} \frac{\partial}{\partial x} \right) \qquad (58)$$

and a similar expression for $\widehat{L}_y$. As a result, even the application of simple finite-difference schemes for equations of the type (49)

$$\left(1 + \bar{\nu}_l \left(\widehat{L}_x + \widehat{L}_y\right)\right) \tilde{\varphi}^{(l+1)}$$
$$= \left(1 + \bar{\mu}_l \left(\widehat{L}_x + \widehat{L}_y\right)\right) \tilde{\varphi}^{(l)}, \qquad (59)$$

derived from Padé approximations of the propagator (54), requires solving systems of linear equations with block-tridiagonal matrices [145]. Although the matrices of such systems are sparse, they require more complex solution methods compared to simple systems with tridiagonal matrices. Another major problem is the size of these matrices, since if there are N_x grid nodes along the x-axis and N_y nodes along the y-axis, then the total number of equations is $N_x N_y$, with a full matrix size of $N_x^2 N_y^2$. For example, in typical medical ultrasound problems, the number of equations $N_x N_y$ can reach several million, which makes direct solution of the system extremely difficult. For this reason, iterative methods are being developed to solve systems of this type [146], which, however, introduce additional challenges related to scheme stability, convergence rate, and the selection of a good initial approximation for the pressure field [147]. Due to the complexity of iterative methods, alternative approaches are being explored for constructing numerical schemes for the three-dimensional wide-angle parabolic equation.

It is worth noting that the method of separation of variables does not directly work for Eq. (59), since the left-hand side of the equation acts on the unknown field $\tilde{\varphi}^{(l+1)}$ using the operator $\widehat{L}_x + \widehat{L}_y$, which contains a sum of derivatives along the mutually perpendicular axes x and y, leading to the emergence of a zeroth-order error when attempting to separate the operators. To compensate for this error directly in Eq. (59), an iterative scheme with corrective terms is known, but it has drawbacks and, for certain values of grid parameters and Padé approximations, becomes unstable [148]. Therefore, most methods for solving the three-dimensional wide-angle parabolic equation rely on the concept of operator splitting. For example, the exact propagator is often decomposed into three propagators [149]:

$$\widehat{H} \approx \exp\left[\zeta\left(\widehat{Q}_x - 1\right)\right] \exp\left[\zeta\left(\widehat{Q}_y - 1\right)\right] \times \exp\left[\zeta\left(1 + \widehat{Q} - \widehat{Q}_x - \widehat{Q}_y\right)\right]. \qquad (60)$$

Here, the notation for the pseudodifferential operators $\widehat{Q}_x = \sqrt{1 + \widehat{L}_x}$ and $\widehat{Q}_y = \sqrt{1 + \widehat{L}_y}$ is introduced, acting separately along the x and y axes. The calculation of the first two operators is performed using the fractional-step Padé method and does not pose difficulties, since each of them is a one-way propagator of a two-dimensional problem and contains only one-dimensional differential operators along individual directions x and y. The remaining third operator is usually expanded into a Taylor series

up to a given order for explicit computation, forming a set of cross operators of the type $\widehat{L}_x^a \widehat{L}_y^b$, where $a > 0$, $b > 0$ are integer powers. In these cross terms, in general, it is necessary to track the order of operators $\widehat{L}_x$ and $\widehat{L}_y$ in the product, since they do not commute with each other in an arbitrary inhomogeneous medium. Since the Taylor series has a limited radius of convergence, this scheme additionally requires the implementation of spatial filters to suppress artificially generated growing components of the wave field. There are also other similar variants of exact propagator splitting that differ in the representation of the cross-term decomposition [133, 150]. Thus, splitting schemes are quite complex to implement and usually require considering a large number of different operator terms.

5.2. A New Method for Approximating the Propagator of the One-Way Wave Equation Based on Fourier Series

Due to the aforementioned computational difficulties arising in the theory of three-dimensional wide-angle parabolic equations, the LIMU laboratory is currently developing alternative methods for constructing wide-angle parabolic models, which, in some respects, are simpler than existing counterparts.

The main idea of the new method is to abandon traditional Padé approximations of the propagator (54) and instead use the expansion of the propagator function into a finite Fourier series within a certain finite window along the eigenvalue axis ξ [151]:

$$H(\xi, \zeta) \approx \sum_{k=-N}^{N} A_k e^{iB_k \xi}. \tag{61}$$

Here, A_k are the complex amplitudes of the Fourier expansion, while $B_k = 2\pi k/\xi_L$ are the corresponding "frequencies" of the discrete spectrum for a window width of ξ_L. The values B_k are neither spatial nor temporal frequencies but simply represent a set of dimensionless numbers spaced apart by a step of $2\pi/\xi_L$ defined by the expansion window width. Replacing ξ back with the operator $\widehat{L}$ allows obtaining the representation of the one-way equation propagator in the form of a Fourier operator series [152]:

$$\widehat{H} \approx \widehat{H}_F = \sum_{k=-N}^{N} A_k e^{iB_k \widehat{L}}. \tag{62}$$

In the aforementioned work [151], the Fourier expansion of the propagator was an intermediate step for smoothing the propagator function, followed by constructing an explicit scheme based on the Taylor series. As a result, on the one hand, a satisfactory approximation of the spectra of both propagating and nonpropagating waves was achieved, while on the other hand, the propagator was smoothed in the vicinity of $\xi = -1$. Here, however, the main advantage of using this form of propagator representation is that each term in the Fourier series is a simple exponential propagator

$$\widehat{H}_E = e^{iB_k \widehat{L}}, \tag{63}$$

which, in its structure, is completely analogous to the propagator of the standard parabolic Eq. (45):

$$\widehat{H}_P = e^{\zeta/2\widehat{L}}. \tag{64}$$

The only difference lies in the coefficients preceding the operator $\widehat{L}$: $\zeta/2$ for the parabolic equation and iB_k for the exponentials in the Fourier operator series. It is also worth noting that the kth positive or negative exponential in the series can be computed by repeating k times the computation of the exponential for the first frequency of the spectrum $B_{\pm 1}$:

$$e^{iB_k \widehat{L}} = \left(e^{iB_1 \widehat{L}}\right)^k. \tag{65}$$

Therefore, the entire operator series (62) can be fully computed with N repeated evaluations of the exponential with positive frequency B_1 and the same number for the exponential with negative frequency B_{-1}:

$$\varphi^{m+1} = \sum_{k=-N}^{N} A_k \tilde{\varphi}_k, \tag{66}$$

where the initial field is $\tilde{\varphi}_0 = \varphi^m$, and the intermediate fields are computed as $\tilde{\varphi}_k = \exp\left(iB_{\pm 1}\widehat{L}\right)\tilde{\varphi}_{k\mp 1}$ with B_1 for $k > 0$ and B_{-1} for $k < 0$.

Various operator splitting schemes, which have a relatively simple structure, can be used to compute the exponential propagators (63) in the three-dimensional problem. For instance, if it is necessary to separate the operators $\widehat{L}_x$ and $\widehat{L}_y$, first- and second-order splitting schemes can be applied:

$$\begin{gathered} e^{iB_1\widehat{L}_x + iB_1\widehat{L}_y} \approx e^{iB_1\widehat{L}_x} e^{iB_1\widehat{L}_y}, \\ e^{iB_1\widehat{L}_x + iB_1\widehat{L}_y} \approx e^{iB_1/2\widehat{L}_x} e^{iB_1\widehat{L}_y} e^{iB_1/2\widehat{L}_x}. \end{gathered} \tag{67}$$

Each exponential containing a separate operator $\widehat{L}_x$ or $\widehat{L}_y$ can then be expanded using Padé approximations of various orders [153], leading to equations of the form:

$$\begin{gathered} \left(1 + \nu_{l,x}\widehat{L}_x\right)\tilde{\varphi}_1 = \left(1 + \mu_{l,x}\widehat{L}_x\right)\tilde{\varphi}_0, \\ \left(1 + \nu_{l,y}\widehat{L}_y\right)\tilde{\varphi}_2 = \left(1 + \mu_{l,y}\widehat{L}_y\right)\tilde{\varphi}_1, \end{gathered} \tag{68}$$

where $\tilde{\varphi}_0$ is the known field at the given step, $\tilde{\varphi}_1$ is an intermediate field, $\tilde{\varphi}_2$ is the field to be computed, and $\nu_{l,x}$, $\mu_{l,x}$, $\nu_{l,y}$, $\mu_{l,y}$ are the corresponding sets of Padé approximation coefficients. For example, applying a first-order splitting scheme together with a diagonal Padé $(1,1)$ approximation for the exponential (64) forms the basis of the standard alternating direction implicit (ADI) scheme for the narrow-angle parabolic equation:

$$\varphi^{m+1} = \left(\frac{1+\zeta/4\widehat{L}_x}{1-\zeta/4\widehat{L}_x}\right)\left(\frac{1+\zeta/4\widehat{L}_y}{1-\zeta/4\widehat{L}_y}\right)\varphi^m, \quad (69)$$

which is also applicable to the propagator $\exp\left(iB_{\pm 1}\widehat{L}\right)$.

Another method for computing operator exponentials involves separating the differential operators and the functions describing inhomogeneities in the operator $\widehat{L}$ [154]. For instance, in a medium with constant density but inhomogeneous refractive index, the following expression can be written:

$$\widehat{L} = \widehat{L}_0 + n_a^2 - 1, \quad (70)$$

where the Laplacian operator $k_0^2\widehat{L}_0 = \partial^2/\partial x^2 + \partial^2/\partial y^2$ includes only derivatives with respect to transverse coordinates. Then, for the operator exponential, the first-order splitting scheme takes the following form:

$$e^{iB_1\left(\widehat{L}_0+n_a^2-1\right)} \approx e^{iB_1\widehat{L}_0}e^{iB_1\left(n_a^2-1\right)}. \quad (71)$$

The first exponential, similar to the angular spectrum method, can be computed in the spatial spectrum using the FFT algorithm, while the second exponential is incorporated as a scalar function of spatial coordinates. This method is widely known in the literature as the split-step-Fourier (SSF) method and has been frequently used to solve the standard parabolic equation in inhomogeneous media [132]. As in the case of separating the operators $\widehat{L}_x$ and $\widehat{L}_y$, higher-order splitting schemes can also be applied here [155].

The main challenge in representing the propagator as an operator Fourier series (62) is that the function $H(\xi,\zeta)$ is not periodic in any finite window along the ξ axis and exhibits a singularity with unbounded derivatives at $\xi = -1$, which marks the boundary between the spectra of propagating and nonpropagating waves. Thus, if no corrective measures are taken, the Fourier series converges slowly, and the Gibbs oscillations become pronounced, rendering the entire scheme unstable. This occurs because certain regions on the ξ axis exhibit values of $|H(\xi,\zeta)|$ exceeding unity to such an extent that the corresponding angular spectrum components grow rapidly when the propagator is applied stepwise along the z axis. To address this issue, it was proposed to first construct a sufficiently smooth modified propagator, which is then expanded into a rapidly converging Fourier series with negligibly small Gibbs oscillations.

The idea of constructing the modified propagator $H_M(\xi,\zeta)$ consists in first selecting a certain spectral interval $[\xi_B,\ \xi_C]$, in which the modified propagator is represented exactly. That is, in this interval, the function $H_M(\xi,\zeta)$, describing the modified propagator, is exactly equal to $H(\xi,\zeta)$. The left boundary of the interval $-1 < \xi_B < 0$, located in the spectral region of propagating waves, determines the angular range of the wide-angle model according to $\theta_{\max} = \arcsin\sqrt{-\xi_B}$. The right boundary of the interval $\xi_C > 0$ is located in the region necessary for describing cases with refractive index inhomogeneities $n_a > 1$. Outside the interval $[\xi_B,\ \xi_C]$, but within the periodic window $[-\xi_L/2,\ \xi_L/2]$ of width ξ_L, other points are located, for example, $-\xi_L/2 < \xi_A < \xi_B$ and $\xi_D = \xi_L/2$, at which the values and derivatives of the exact and modified propagators are matched. In the interval between the pairs of points ξ_C and ξ_D, ξ_A and ξ_B, a two-point Hermite interpolation of a given order is performed, which ensures continuity not only of the function values but also of its derivatives up to the corresponding order $N_d \geq 1$. Thus, in the periodic window $[-\xi_L/2,\ \xi_L/2]$, the modified propagator and its derivatives up to the specified N_d remain continuous functions, which significantly increases the convergence rate of the Fourier series. At the same time, in the interval $[\xi_B,\ \xi_C]$, the required exact values of the propagator are preserved, while outside this interval $|H_M(\xi,\zeta)| < 1$, which ensures the attenuation of unwanted components of the spatial spectrum of the pressure field. In Figs. 6a and 6b an example of the modified propagator (amplitude and phase) for $|\zeta| = 1$ with a maximum angle $\theta_{\max} = 60^\circ$ is shown when expanded in a window of width $\xi_L = 4$. Here, three consecutive periods are shown, among which the period in the interval $[-2\ 2]$, bounded by vertical dashed lines in the figure, covers the region of ξ values of interest for the exact propagator. In this example, Hermite interpolation with $N_d = 5$ was used, which allowed reducing the amplitude of Gibbs oscillations at a harmonic number $2N = 100$ to the level of 10^{-8} (Fig. 6c). The phase error in this case is somewhat larger and amounts to 10^{-7} (Fig. 6d). In practice, such a low amplitude of oscillations prevents the scheme from diverging even when modeling the field at distances of up to thousands of wavelengths. Moreover, the modified propagator can be constructed in various ways, for example, by separately matching the amplitude and phase, and varying the free parameters to reduce the

number of Fourier harmonics for a given approximation error level [156]. It is important to note that due to the periodicity of the Fourier expansion of the propagator, some components of the spatial spectrum with high frequencies from the nonpropagating wave region have a transmission coefficient equal to that in the propagating wave region, i.e., equal to unity (excluding the effect of Gibbs oscillations). If suppression of these components is required, additional low-pass spatial filters may be applied [157].

Thus, in new theoretical studies conducted at the LIMU laboratory on the topic of numerical modeling of wave propagation in inhomogeneous media, alternative methods of the wide-angle parabolic equation are being developed, aimed at obtaining one-way three-dimensional models to which sufficiently simple numerical schemes can be applied, eliminating the need to solve systems of linear equations with large sparse matrices or to compute a large number of combinations of cross-operators considering their commutative properties. The proposed method of modifying the exact propagator followed by its expansion into a finite Fourier series allows constructing various versions of numerical schemes, including those using finite difference or finite element methods, as well as exponential operator splitting methods with the possibility of performing computations in the spatial spectrum based on the FFT algorithm.

CONCLUSIONS

This review includes a description of the main numerical algorithms developed over the past three decades at the Laboratory for Industrial and Medical Ultrasound of Lomonosov Moscow State University for solving nonlinear problems of diffracting acoustic wave propagation and confined beams in absorbing and inhomogeneous media. The theoretical foundation for the algorithms is formed by classical evolutionary equations of nonlinear acoustics, such as the Burgers equation, the Khokhlov–Zabolotskaya–Kuznetsov (KZK) equation, the one-way Westervelt equation, and their generalizations for various absorption and dispersion laws, as well as inhomogeneous media. Examples of results obtained in numerical experiments for various practical problems of nonlinear acoustics in medical ultrasound, aeroacoustics, and the analysis of nonlinear parametric interactions of intense pump waves at close frequencies are presented, demonstrating the capabilities of the discussed methods. A new approach to constructing a wide-angle parabolic model suitable for describing one-way wave propagation in three-dimensional inhomogeneous media is also outlined.

The numerical models and their software implementations presented in this review allow for further development and generalization to a broader range of problems. One of the drawbacks of existing algorithms is the relatively low computation speed in three-dimensional problems when strong nonlinear effects are present. One possible solution here is using the advantages of parallel computing on graphics processors. However, the main challenge lies in the fact that, unlike parallelization methods on central processors, such as those utilizing code extensions provided by the OpenMP standard, no unified standard currently exists in GPU computing that ensures compatibility with existing code bases. Moreover, relatively ready-to-use solutions are offered by only one well-known graphics chip manufacturer, creating the risk of dependency on a single vendor of proprietary software and hardware solutions. Regarding the physical problems for which these models are being developed, applications where medium inhomogeneities significantly influence wave propagation are becoming increasingly relevant. For example, considerable attention is currently being given to research on noninvasive ultrasound surgery methods for tumor destruction in abdominal organs (liver, kidney, pancreas), where heterogeneous layers of abdominal wall tissues along the path to the focal point create strong distortions (aberrations) of the ultrasound beam. The development of one-way models based on the wide-angle parabolic approximation for studying these processes and the possibilities for aberration correction is therefore a highly relevant research direction.

FUNDING

This work was supported by the Russian Science Foundation (grant no. 23-22-00220).

CONFLICT OF INTEREST

The authors of this work declare that they have no conflicts of interest.

REFERENCES

1. M. B. Vinogradova, O. V. Rudenko, and A. P. Sukhorukov, *Wave Theory: Linear and Nonlinear Waves* (Lenand, Moscow, 2019).
2. B. E. Treeby and B. T. Cox, J. Biomed. Opt. **15**, 021314 (2010). https://doi.org/10.1117/1.3360308
3. O. V. Rudenko and S. I. Soluyan, *Theoretical Foundations of Nonlinear Acoustics* (Nauka, Moscow, 1975).
4. E. A. Zabolotskaya and R. V. Khokhlov, Acoust. Phys. **15**, 40 (1969).
5. P. J. Westervelt, J. Acoust. Soc. Am. **35**, 535 (1963). https://doi.org/10.1121/1.1918525

6. V. E. Ostashev, D. K. Wilson, and M. B. Muhlestein, J. Acoust. Soc. Am. **147**, 3969 (2020). https://doi.org/10.1121/10.0001397
7. T. Kamakura, H. Nomura, and G. T. Clement, Ultrasonics **53**, 432 (2013). https://doi.org/10.1016/j.ultras.2012.08.008
8. A. G. Tyshchenko, S. B. Kozitskii, M. S. Kazak, and P. S. Petrov, Acoust. Phys. **69**, 710 (2023). https://doi.org/10.1134/s1063771023600316
9. M. Yu. Trofimov, Acoust. Phys. **48**, 728 (2002).
10. K. V. Avilov and N. E. Mal'tsev, Akust. Zh. **27**, 335 (1981).
11. M. D. Collins and W. L. Siegmann, J. Theor. Comput. Acoust. **29**, 2130003 (2021). https://doi.org/10.1142/s2591728521300038
12. N. M. Ryskin and D. I. Trubetskov, *Nonlinear Waves* (Lenand, Moscow, 2021).
13. A. L. Polyakova, S. I. Soluyan, and R. V. Khokhlov, Sov. Phys. Acoust. **8**, 78 (1962).
14. Y.-S. Lee and M. F. Hamilton, J. Acoust. Soc. Am. **97**, 906 (1995). https://doi.org/10.1121/1.412135
15. R. I. McLachlan and G. R. W. Quispel, in *Acta Numerica 2002*, Ed. by A. Iserles (Cambridge University Press, 2002), Vol. 11, p. 341. https://doi.org/10.1017/cbo9780511550140.005
16. S. S. Kashcheeva, O. A. Sapozhnikov, V. A. Khokhlova, M. A. Averkiou, and L. A. Crum, Acoust. Phys. **46**, 170 (2000).
17. Yu. A. Pishchal'nikov, O. A. Sapozhnikov, and V. A. Khokhlova, Acoust. Phys. **42**, 362 (1996).
18. A. Kurganov and E. Tadmor, J. Comput. Phys. **160**, 241 (2000). https://doi.org/10.1006/jcph.2000.6459
19. E. O. Konnova, V. A. Khokhlova, and P. V. Yuldashev, Acoust. Phys. **68**, 529 (2022). https://doi.org/10.1134/s1063771022060161
20. J. N. Tjotta, S. Tjotta, and E. H. Vefring, J. Acoust. Soc. Am. **89**, 1017 (1991). https://doi.org/10.1121/1.400523
21. D. J. Thomson and N. R. Chapman, J. Acoust. Soc. Am. **74**, 1848 (1983). https://doi.org/10.1121/1.390272
22. J. E. Soneson, J. Acoust. Soc. Am. **131**, EL481 (2012). https://doi.org/10.1121/1.4722170
23. J. Tavakkoli, D. Cathignol, R. Souchon, and O. A. Sapozhnikov, J. Acoust. Soc. Am. **104**, 2061 (1998). https://doi.org/10.1121/1.423720
24. R. J. Zemp, J. Tavakkoli, and R. S. C. Cobbold, J. Acoust. Soc. Am. **113**, 139 (2003). https://doi.org/10.1121/1.1528926
25. V. A. Khokhlova, A. E. Ponomarev, M. A. Averkiou, and L. A. Crum, Acoust. Phys. **52**, 481 (2006). https://doi.org/10.1134/s1063771006040178
26. J. W. Goodman, *Introduction to Fourier Optics* (McGraw-Hill, New York, 1996).
27. J. Blackmore, R. O. Cleveland, and J. Mobley, J. Acoust. Soc. Am. **144**, 2947 (2018). https://doi.org/10.1121/1.5079637
28. P. T. Christopher and K. J. Parker, J. Acoust. Soc. Am. **90**, 507 (1991). https://doi.org/10.1121/1.401277
29. K. V. Avilov, Acoust. Phys. **41**, 1 (1995).
30. P. V. Yuldashev, I. S. Mezdrokhin, and V. A. Khokhlova, Acoust. Phys. **64**, 309 (2018). https://doi.org/10.1134/s1063771018030168
31. G. H. Brooke, D. J. Thomson, and G. R. Ebbeson, Journal of Computational Acoustics **9**, 69 (2001). https://doi.org/10.1142/s0218396x01000425
32. M. D. Collins, J. Acoust. Soc. Am. **93**, 1736 (1993). https://doi.org/10.1121/1.406739
33. D. Yevick and D. J. Thomson, J. Acoust. Soc. Am. **108**, 2784 (2000). https://doi.org/10.1121/1.1322571
34. E. O. Konnova, P. V. Yuldashev, and V. A. Khokhlova, Bull. Russ. Acad. Sci.: Phys. **85**, 632 (2021). https://doi.org/10.3103/s1062873821060125
35. L. R. Gavrilov, *High Intensity Focused Ultrasound in Medicine* (Fazis, Moscow, 1967).
36. M. R. Bailey, V. A. Khokhlova, O. A. Sapozhnikov, S. G. Kargl, and L. A. Crum, Acoust. Phys. **49**, 369 (2003). https://doi.org/10.1134/1.1591291
37. *Physical Principles of Medical Ultrasonics*, Ed. by C. R. Hill, J. C. Bamber, and G. R. ter Haar (Wiley, 2004). https://doi.org/10.1002/0470093978
38. L. A. Crum, M. Canney, M. Bailey, T. Khokhlova, V. Khokhlova, O. Sapozhnikov, W. Kreider, and J. Simon, Med. Phys. **38**, 3811 (2011). https://doi.org/10.1118/1.3613352
39. A. Maxwell, O. Sapozhnikov, M. Bailey, L. Crum, Zh. Xu, B. Fowlkes, Ch. Cain, and V. Khokhlova, Acoustics Today **8** (4), 24 (2012). https://doi.org/10.1121/1.4788649
40. O. V. Bessonova and V. Wilkens, IEEE Trans. Ultrason., Ferroelectr. Freq. Control **60**, 290 (2013). https://doi.org/10.1109/tuffc.2013.2565
41. T. D. Khokhlova, M. S. Canney, V. A. Khokhlova, O. A. Sapozhnikov, L. A. Crum, and M. R. Bailey, J. Acoust. Soc. Am. **130**, 3498 (2011). https://doi.org/10.1121/1.3626152
42. E. A. Filonenko and V. A. Khokhlova, Akust. Zh. **47**, 541 (2001).
43. M. S. Canney, M. R. Bailey, L. A. Crum, V. A. Khokhlova, and O. A. Sapozhnikov, J. Acoust. Soc. Am. **124**, 2406 (2008). https://doi.org/10.1121/1.2967836
44. W. Kreider, P. V. Yuldashev, O. A. Sapozhnikov, N. Farr, A. Partanen, M. R. Bailey, and V. A. Khokhlova, IEEE Trans. Ultrason., Ferroelectr. Freq. Control **60**, 1683 (2013). https://doi.org/10.1109/tuffc.2013.2750

45. P. V. Yuldashev and V. A. Khokhlova, Acoust. Phys. **57**, 334 (2011). https://doi.org/10.1134/s1063771011030213
46. E. M. Ponomarchuk, P. V. Yuldashev, D. A. Nikolaev, S. A. Tsysar, A. A. Mironova, and V. A. Khokhlova, Acoust. Phys. **69**, 459 (2023). https://doi.org/10.1134/s1063771023600560
47. O. A. Sapozhnikov, S. A. Tsysar, V. A. Khokhlova, and W. Kreider, J. Acoust. Soc. Am. **138**, 1515 (2015). https://doi.org/10.1121/1.4928396
48. S. A. Tsysar, Y. D. Sinelnikov, and O. A. Sapozhnikov, Acoust. Phys. **57**, 94 (2011). https://doi.org/10.1134/s1063771011010167
49. O. A. Sapozhnikov, A. E. Ponomarev, and M. A. Smagin, Acoust. Phys. **52**, 324 (2006). https://doi.org/10.1134/s1063771006030134
50. O. A. Sapozhnikov, Yu. A. Pishchal'nikov, and A. V. Morozov, Acoust. Phys. **49**, 354 (2003). https://doi.org/10.1134/1.1574364
51. S. A. Tsysar, D. A. Nikolaev, and O. A. Sapozhnikov, Acoust. Phys. **67**, 320 (2021). https://doi.org/10.1134/s1063771021030131
52. A. Z. Kaloev, D. A. Nikolaev, V. A. Khokhlova, S. A. Tsysar, and O. A. Sapozhnikov, Acoust. Phys. **68**, 71 (2022). https://doi.org/10.1134/s1063771022010043
53. D. A. Nikolaev, S. A. Tsysar, and O. A. Sapozhnikov, Bull. Russ. Acad. Sci.: Phys. **85**, 658 (2021). https://doi.org/10.3103/s1062873821060150
54. F. A. Nartov, R. P. Williams, and V. A. Khokhlova, Acoust. Phys. **70**, 165 (2024). https://doi.org/10.1134/S1063771023601292
55. S. Tsysar, W. Kreider, and O. Sapozhnikov, Proceedings of Meetings on Acoustics **19**, 55015 (2013). https://doi.org/10.1121/1.4800403
56. S. A. Tsysar, P. B. Rosnitskiy, S. A. Asfandiyarov, S. A. Petrosyan, V. A. Khokhlova, and O. A. Sapozhnikov, Acoust. Phys. **70**, 82 (2024). https://doi.org/10.1134/S1063771023601280
57. D. A. Nikolaev, S. A. Tsysar, V. A. Khokhlova, W. Kreider, and O. A. Sapozhnikov, J. Acoust. Soc. Am. **149**, 386 (2021). https://doi.org/10.1121/10.0003212
58. A. D. Maxwell, P. V. Yuldashev, W. Kreider, T. D. Khokhlova, G. R. Schade, T. L. Hall, O. A. Sapozhnikov, M. R. Bailey, and V. A. Khokhlova, IEEE Trans. Ultrason., Ferroelectr. Freq. Control **64**, 1542 (2017). https://doi.org/10.1109/tuffc.2017.2739649
59. Ch. R. Bawiec, P. B. Rosnitskiy, A. T. Peek, A. D. Maxwell, W. Kreider, G. R. ter Haar, O. A. Sapozhnikov, V. A. Khokhlova, and T. D. Khokhlova, IEEE Trans. Ultrason., Ferroelectr. Freq. Control **68**, 2884 (2021). https://doi.org/10.1109/tuffc.2021.3073347
60. M. M. Karzova, P. V. Yuldashev, O. A. Sapozhnikov, V. A. Khokhlova, B. W. Cunitz, W. Kreider, and M. R. Bailey, J. Acoust. Soc. Am. **141**, 2327 (2017). https://doi.org/10.1121/1.4979261
61. M. M. Karzova, P. V. Yuldashev, V. A. Khokhlova, F. A. Nartov, K. P. Morrison, and T. D. Khokhlova, IEEE Trans. Ultrason., Ferroelectr. Freq. Control **68**, 2930 (2021). https://doi.org/10.1109/tuffc.2021.3070528
62. R. P. Williams, M. M. Karzova, P. V. Yuldashev, A. Z. Kaloev, F. A. Nartov, V. A. Khokhlova, B. W. Cunitz, K. P. Morrison, and T. D. Khokhlova, IEEE Trans. Ultrason., Ferroelectr. Freq. Control **70**, 693 (2023). https://doi.org/10.1109/tuffc.2023.3268603
63. P. B. Rosnitskiy, P. V. Yuldashev, O. A. Sapozhnikov, L. R. Gavrilov, and V. A. Khokhlova, J. Acoust. Soc. Am. **146**, 1786 (2019). https://doi.org/10.1121/1.5126685
64. P. V. Yuldashev, S. M. Shmeleva, S. A. Ilyin, O. A. Sapozhnikov, L. R. Gavrilov, and V. A. Khokhlova, Phys. Med. Biol. **58**, 2537 (2013). https://doi.org/10.1088/0031-9155/58/8/2537
65. P. V. Yuldashev, M. M. Karzova, W. Kreider, P. B. Rosnitskiy, O. A. Sapozhnikov, and V. A. Khokhlova, IEEE Trans. Ultrason., Ferroelectr. Freq. Control **68**, 2837 (2021). https://doi.org/10.1109/tuffc.2021.3074611
66. C. Perez, H. Chen, T. J. Matula, M. Karzova, and V. A. Khokhlova, J. Acoust. Soc. Am. **134**, 1663 (2013). https://doi.org/10.1121/1.4812885
67. A. G. Musatov, O. V. Rudenko, and O. A. Sapozhnikov, Sov. Phys. Acoust. **38**, 274 (1992).
68. K. A. Naugolnykh and E. V. Romanenko, Sov. Phys. Acoust. **5**, 191 (1959).
69. O. V. Bessonova, V. A. Khokhlova, M. R. Bailey, M. S. Canney, and L. A. Crum, Acoust. Phys. **55**, 463 (2009). https://doi.org/10.1134/s1063771009040034
70. O. V. Rudenko and O. A. Sapozhnikov, Phys.-Usp. **47**, 907 (2004). https://doi.org/10.1070/pu2004v047n09abeh001865
71. M. M. Karzova, M. V. Averiyanov, O. A. Sapozhnikov, and V. A. Khokhlova, Acoust. Phys. **58**, 81 (2012). https://doi.org/10.1134/s1063771011060078
72. P. B. Rosnitskiy, P. V. Yuldashev, and V. A. Khokhlova, Acoust. Phys. **61**, 301 (2015). https://doi.org/10.1134/s1063771015030148
73. P. B. Rosnitskiy, P. V. Yuldashev, B. A. Vysokanov, and V. A. Khokhlova, Acoust. Phys. **62**, 151 (2016). https://doi.org/10.1134/s1063771016020123
74. P. B. Rosnitskiy, P. V. Yuldashev, O. A. Sapozhnikov, A. D. Maxwell, W. Kreider, M. R. Bailey, and V. A. Khokhlova, IEEE Trans. Ultrason., Ferroelectr. Freq. Control **64**, 374 (2017). https://doi.org/10.1109/tuffc.2016.2619913

75. V. A. Khokhlova, P. V. Yuldashev, P. B. Rosnitskiy, A. D. Maxwell, W. Kreider, M. R. Bailey, and O. A. Sapozhnikov, Phys. Procedia **87**, 132 (2016). https://doi.org/10.1016/j.phpro.2016.12.020
76. M. M. Karzova, P. V. Yuldashev, P. B. Rosnitskiy, and V. A. Khokhlova, Bull. Russ. Acad. Sci.: Phys. **81**, 927 (2017). https://doi.org/10.3103/s1062873817080135
77. P. B. Rosnitskiy, L. R. Gavrilov, P. V. Yuldashev, O. A. Sapozhnikov, and V. A. Khokhlova, Acoust. Phys. **63**, 531 (2017). https://doi.org/10.1134/s1063771017050104
78. A. A. Krokhmal, D. A. Nikolaev, S. A. Tsysar, and O. A. Sapozhnikov, Acoust. Phys. **66**, 449 (2020). https://doi.org/10.1134/s1063771020050061
79. B. Sturtevant and V. A. Kulkarny, J. Fluid Mech. **73**, 651 (1976). https://doi.org/10.1017/s0022112076001559
80. M. M. Karzova, V. A. Khokhlova, E. Salze, S. Ollivier, and P. Blanc-Benon, J. Acoust. Soc. Am. **137**, EL436 (2015). https://doi.org/10.1121/1.4921681
81. O. V. Rudenko and Yu. N. Makov, Acoust. Phys. **67**, 1 (2021). https://doi.org/10.1134/s1063771021010036
82. T. Feder, Phys. Today **60** (4), 24 (2007). https://doi.org/10.1063/1.2731962
83. A. D. Pierce and D. J. Maglieri, J. Acoust. Soc. Am. **51**, 702 (1972). https://doi.org/10.1121/1.1912904
84. V. I. Tatarskii, *Wave Propagation in a Turbulent Atmosphere* (Nauka, Moscow, 1967).
85. A. N. Dubrovskii, O. V. Rudenko, and V. A. Khokhlova, Acoust. Phys. **42**, 550 (1996).
86. M. F. Hamilton, V. A. Khokhlova, and O. V. Rudenko, J. Acoust. Soc. Am. **101**, 1298 (1997). https://doi.org/10.1121/1.418158
87. P. V. Yuldashev, N. A. Bryseva, M. V. Averiyanov, P. H. Blanc-Benon, and V. A. Khokhlova, Acoust. Phys. **56**, 158 (2010). https://doi.org/10.1134/s1063771010020065
88. F. Coulouvrat, Wave Motion **49**, 50 (2012). https://doi.org/10.1016/j.wavemoti.2011.07.002
89. A. N. Carr, J. B. Lonzaga, and S. A. E. Miller, J. Sound Vib. **571**, 118118 (2024). https://doi.org/10.1016/j.jsv.2023.118118
90. M. V. Aver'yanov, V. A. Khokhlova, O. A. Sapozhnikov, P. H. Blanc-Benon, and R. O. Cleveland, Acoust. Phys. **52**, 623 (2006). https://doi.org/10.1134/s1063771006060017
91. M. Averiyanov, P. Blanc-Benon, R. O. Cleveland, and V. Khokhlova, J. Acoust. Soc. Am. **129**, 1760 (2011). https://doi.org/10.1121/1.3557034
92. P. V. Yuldashev, S. Ollivier, M. M. Karzova, V. A. Khokhlova, and P. Blanc-Benon, J. Acoust. Soc. Am. **142**, 3402 (2017). https://doi.org/10.1121/1.5015991
93. M. Averiyanov, S. Ollivier, V. Khokhlova, and P. Blanc-Benon, J. Acoust. Soc. Am. **130**, 3595 (2011). https://doi.org/10.1121/1.3652869
94. É. Salze, P. Yuldashev, S. Ollivier, V. Khokhlova, and P. Blanc-Benon, J. Acoust. Soc. Am. **136**, 556 (2014). https://doi.org/10.1121/1.4887458
95. P. V. Yuldashev, M. V. Averiyanov, V. A. Khokhlova, S. Ollivier, and P. H. Blanc-Benon, Acoust. Phys. **54**, 32 (2008). https://doi.org/10.1134/s1063771008010065
96. D. Luquet, R. Marchiano, and F. Coulouvrat, J. Comput. Phys. **379**, 237 (2019). https://doi.org/10.1016/j.jcp.2018.11.041
97. P. V. Yuldashev, M. M. Karzova, V. A. Khokhlova, and P. H. Blanc-Benon, Acoust. Phys. **67**, 26 (2021). https://doi.org/10.1134/s1063771021010061
98. R. A. Lee and J. M. Downing, J. Acoust. Soc. Am. **99**, 768 (1996). https://doi.org/10.1121/1.414654
99. P. Yuldashev, S. Ollivier, M. Averiyanov, O. Sapozhnikov, V. Khokhlova, and P. Blanc-Benon, J. Acoust. Soc. Am. **128**, 3321 (2010). https://doi.org/10.1121/1.3505106
100. M. M. Karzova, P. V. Yuldashev, V. A. Khokhlova, S. Ollivier, E. Salze, and P. Blanc-Benon, J. Acoust. Soc. Am. **137**, 3244 (2015). https://doi.org/10.1121/1.4921026
101. P. Yuldashev, M. Karzova, V. Khokhlova, S. Ollivier, and P. Blanc-Benon, J. Acoust. Soc. Am. **137**, 3314 (2015). https://doi.org/10.1121/1.4921549
102. Z. J. Zhou, L. Rufer, E. Salze, P. Yuldashev, S. Ollivier, and M. Wong, J. Micromech. Microeng. **23**, 105006 (2013). https://doi.org/10.1088/0960-1317/23/10/105006
103. M. M. Karzova, P. V. Yuldashev, V. A. Khokhlova, S. Ollivier, and P. H. Blanc-Benon, Bull. Russ. Acad. Sci.: Phys. **79**, 1293 (2015). https://doi.org/10.3103/s1062873815100123
104. C. Desjouy, S. Ollivier, O. Marsden, M. Karzova, and P. Blanc-Benon, Phys. Fluids **28**, 27102 (2016). https://doi.org/10.1063/1.4940987
105. M. M. Karzova, T. Lechat, S. Ollivier, D. Dragna, P. V. Yuldashev, V. A. Khokhlova, and P. Blanc-Benon, J. Acoust. Soc. Am. **145**, 26 (2019). https://doi.org/10.1121/1.5084266
106. V. A. Zverev, Acoust. Phys. **45**, 611 (1999).
107. B. K. Novikov, O. V. Rudenko, and V. I. Timoshenko, *Nonlinear Hydroacoustics* (Sudostroenie, Leningrad, 1981).
108. H. Zhou, S. H. Huang, and W. Li, Sensors **20**, 2148 (2020). https://doi.org/10.3390/s20072148

109. W.-S. Gan, J. Yang, and T. Kamakura, Appl. Acoust. **73**, 1211 (2012). https://doi.org/10.1016/j.apacoust.2012.04.001
110. S.-Y. Chiou, F. Forsberg, T. B. Fox, and L. Needleman, J. Ultrasound Med. **26**, 1557 (2007). https://doi.org/10.7863/jum.2007.26.11.1557
111. M. B. Moffett, R. H. Mellen, and W. L. Konrad, J. Acoust. Soc. Am. **63**, 1326 (1978). https://doi.org/10.1121/1.381885
112. T. Kamakura, N. Hamada, K. Aoki, and Yo. Kumamoto, J. Acoust. Soc. Am. **85**, 2331 (1989). https://doi.org/10.1121/1.397778
113. J. Naze Tjotta, S. Tjotta, and E. H. Vefring, J. Acoust. Soc. Am. **88**, 2859 (1990). https://doi.org/10.1121/1.399690
114. M. A. Averkiou, Y.-S. Lee, and M. F. Hamilton, J. Acoust. Soc. Am. **94**, 2876 (1993). https://doi.org/10.1121/1.407344
115. J. Zhong, R. Kirby, and X. Qiu, J. Acoust. Soc. Am. **149**, 1524 (2021). https://doi.org/10.1121/10.0003606
116. M. Červenka and M. Bednařík, J. Acoust. Soc. Am. **146**, 2163 (2019). https://doi.org/10.1121/1.5126863
117. T. Kamakura, M. Tani, Y. Kumamoto, and M. A. Breazeale, Acustica **80**, 332 (1994).
118. A. V. Kvashennikova, P. V. Yuldashev, V. A. Khokhlova, and I. B. Esipov, J. Acoust. Soc. Am. **155**, 1682 (2024). https://doi.org/10.1121/10.0025049
119. A. V. Tyurina, P. V. Yuldashev, I. B. Esipov, and V. A. Khokhlova, Acoust. Phys. **69**, 30 (2023). https://doi.org/10.1134/s1063771022700014
120. A. V. Tyurina, P. V. Yuldashev, I. B. Esipov, and V. A. Khokhlova, Acoust. Phys. **68**, 130 (2022). https://doi.org/10.1134/s1063771022020105
121. M. S. Sergeeva, A. V. Tyurina, P. V. Yuldashev, and V. A. Khokhlova, Uchenye Zapiski Fizicheskogo Fakul'teta Moskovskogo Universiteta, No. 4, 2240101 (2022).
122. I. B. Esipov, O. E. Popov, V. A. Voronin, and S. P. Tarasov, Acoust. Phys. **55**, 76 (2009). https://doi.org/10.1134/s1063771009010084
123. T. Varslot and G. Taraldsen, IEEE Trans. Ultrason., Ferroelectr. Freq. Control **52**, 1473 (2005). https://doi.org/10.1109/TUFFC.2005.1516019
124. T. D. Mast, Acoustics Research Letters Online **1** (2), 37 (2000). https://doi.org/10.1121/1.1336896
125. A. S. Bobina, P. B. Rosnitskiy, T. D. Khokhlova, P. V. Yuldashev, and V. A. Khokhlova, Bull. Russ. Acad. Sci.: Phys. **85**, 675 (2021). https://doi.org/10.3103/s1062873821060058
126. A. T. Peek, G. P. L. Thomas, D. F. Leotta, P. V. Yuldashev, V. A. Khokhlova, and T. D. Khokhlova, J. Acoust. Soc. Am. **151**, 3007 (2022). https://doi.org/10.1121/10.0010369
127. D. Lee, A. D. Pierce, and E.-C. Shang, Journal of Computational Acoustics **8**, 527 (2000). https://doi.org/10.1142/s0218396x00000388
128. F. B. Jensen, W. A. Kuperman, M. B. Porter, and H. Schmidt, in *Computational Ocean Acoustics*, Modern Acoustics and Signal Processing (Springer, New York, 2011), p. 457. https://doi.org/10.1007/978-1-4419-8678-8_6
129. E. M. Salomons, *Computational Atmospheric Acoustics* (Springer, Dordrecht, 2001). https://doi.org/10.1007/978-94-010-0660-6
130. O. Ozgun, G. Apaydin, M. Kuzuoglu, and L. Sevgi, Comput. Phys. Commun. **182**, 2638 (2011). https://doi.org/10.1016/j.cpc.2011.07.017
131. M. Kolesik, *Computational Optics: Beam Propagation Methods* (Nova Science, New York, 2017).
132. D. J. Thomson and N. R. Chapman, J. Acoust. Soc. Am. **74**, 1848 (1983). https://doi.org/10.1121/1.390272
133. Y.-T. Lin, J. M. Collis, and T. F. Duda, J. Acoust. Soc. Am. **132**, EL364 (2012). https://doi.org/10.1121/1.4754421
134. M. D. Collins and E. K. Westwood, J. Acoust. Soc. Am. **89**, 1068 (1991). https://doi.org/10.1121/1.400526
135. M. D. Collins and W. L. Siegmann, *Parabolic Wave Equations with Applications* (Springer, New York, 2019). https://doi.org/10.1007/978-1-4939-9934-7
136. W. L. Siegmann, G. A. Kriegsmann, and D. Lee, J. Acoust. Soc. Am. **78**, 659 (1985). https://doi.org/10.1121/1.392434
137. S. T. McDaniel, J. Acoust. Soc. Am. **58**, 1178 (1975). https://doi.org/10.1121/1.380801
138. L. Halpern and L. N. Trefethen, J. Acoust. Soc. Am. **84**, 1397 (1988). https://doi.org/10.1121/1.396586
139. A. Bamberger, B. Engquist, L. Halpern, and P. Joly, SIAM J. Appl. Math. **48**, 129 (1988). https://doi.org/10.1137/0148006
140. M. D. Collins, J. Acoust. Soc. Am. **86**, 1097 (1989). https://doi.org/10.1121/1.398101
141. M. D. Collins, R. J. Cederberg, D. B. King, and S. A. Chin-Bing, J. Acoust. Soc. Am. **100**, 178 (1996). https://doi.org/10.1121/1.415921
142. Ya. Y. Lu, Appl. Numer. Math. **27**, 141 (1998). https://doi.org/10.1016/s0168-9274(98)00009-9
143. K. E. Gilbert and M. J. White, J. Acoust. Soc. Am. **85**, 630 (1989). https://doi.org/10.1121/1.397587
144. M. D. Collins, J. Acoust. Soc. Am. **93**, 1736 (1993). https://doi.org/10.1121/1.406739
145. K. Lee, W. Seong, and Yo. Na, J. Acoust. Soc. Am. **146**, 2050 (2019). https://doi.org/10.1121/1.5125592

146. C. Khodr, M. Azarpeyvand, and D. N. Green, J. Acoust. Soc. Am. **148**, 1089 (2020). https://doi.org/10.1121/10.0001766
147. G. R. Hadley, J. Comput. Phys. **203**, 358 (2005). https://doi.org/10.1016/j.jcp.2004.09.015
148. E. V. Bekker, P. Sewell, T. M. Benson, and A. Vukovic, J. Lightwave Technol. **27**, 2595 (2009). https://doi.org/10.1109/jlt.2009.2013219
149. K. Lee, W. Seong, and Yo. Na, J. Acoust. Soc. Am. **146**, 2041 (2019). https://doi.org/10.1121/1.5125428
150. S. Ivansson, J. Acoust. Soc. Am. **146**, 2030 (2019). https://doi.org/10.1121/1.5125425
151. A. Balkenohl and D. Schulz, J. Lightwave Technol. **32**, 4519 (2014). https://doi.org/10.1109/jlt.2014.2360413
152. P. V. Yuldashev, E. O. Konnova, and V. A. Khokhlova, in *Proceedings of the 35th Session of the Russian Acoustical Society, Moscow, 2023* (GEOS, Moscow, 2023), p. 521. https://doi.org/10.34756/GEOS.2023.17.38421
153. C. Moler and Ch. Van Loan, SIAM Rev. **45**, 3 (2003). https://doi.org/10.1137/s00361445024180
154. Y.-T. Lin and T. F. Duda, J. Acoust. Soc. Am. **132**, EL61 (2012). https://doi.org/10.1121/1.4730328
155. B. Hermansson and D. Yevick, Opt. Lett. **16**, 354 (1991). https://doi.org/10.1364/ol.16.000354
156. E. O. Konnova, P. V. Yuldashev, and V. A. Khokhlova, in *Proceedings of the 34th All-Russian School-Seminar Wave Phenomena: Physics and Applications Dedicated to Professor (Waves-2023)*, Ed. by A. P. Sukhorukov (Moskovskii Gosudarstvennyi Universitet im. M.V. Lomonosova, Fizicheskii Fakul'tet, Moscow, 2023), p. 8.
157. R. J. Cederberg, M. D. Collins, H. Schmidt, and W. L. Siegmann, J. Acoust. Soc. Am. **101**, 2518 (1997). https://doi.org/10.1121/1.418493

AI tools may have been used in the translation or editing of this article.